FAKULTÄT FÜR ELEKTROTECHNIK UND INFORMATIONSTECHNIK
Faculty of Electrical Engineering and Information Technology

Metrological characterization of a translating-coil magnetometer for measuring the field quality in dipole magnets

Master Thesis

carried out for the purpose of obtaining the academic degree of

Master of Science

in the course of the master's program

Elektrotechnik und Informationstechnik

submitted by

Andreas Windischhofer, BSc

Student ID: 01327334

at the faculty of Elektrotechnik und Informationstechnik

part of TU Wien

in cooperation with CERN, Geneva, Switzerland

Supervisor: Dr. Stephan Russenschuck

Vienna, January 2022

Andreas Windischhofer

Affidavit

I declare in lieu of oath, that I wrote this thesis and performed the associated research myself, using only literature cited in this volume. If text passages from sources are used literally, they are marked as such.
I confirm that this work is original and has not been submitted elsewhere for any examination, nor is it currently under consideration for a thesis elsewhere.

Vienna, 31.01.2022

Date

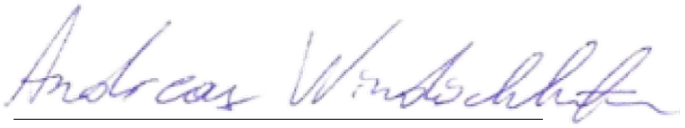

Signature

Acknowledgements

This thesis became possible with the technical student program at CERN. The work was carried out in the magnetic measurement section. I not only gained a lot of new technical knowledge around magnetic measurements, also I got an insight in the scientific world. Due to all the experience that I gathered during my time there, I could grow on a professional level as well as on a personal one.

I would like to express my appreciation to the supervisor of this thesis and head of the magnetic measurement section Dr. Stephan Russenschuck for countless discourses as well as his patient support while I was writing this thesis. Furthermore, I want to thank Dr. Giancarlo Golluccio for his many technical pieces of advice and also his support for my personal growth. Let me also express my gratitude to all members of the team that helped me in their respective field of knowledge.

A cordial thank you goes to all my colleges that also accompanied me in my leisure time. This was an essential balance for me and helped me to master my professional challenges.

Despite the large distance to my hometown Vienna, my family was supportive all the time. Without my parents Ulrike and Wolfgang this adventure wouldn't have gone ahead as it did.

Abstract

The goal of this thesis is to present a novel measurement device, intended for the magnetic field measurement of accelerator magnets. We give a detailed description of the translating-coil magnetometer as an abstract model as well as a system.

Measurements were performed on a reference dipole at CERN. We present the results from the metrological characterization campaign, along with an insight in the calibration procedure, which includes the derivation of systematic corrections. Our study of the results showed that the translating-coil magnetometer is a promising device for magnetic measurement actions.

As underlying measurement principle, the Faraday law is used. It is applied on a coil moving along a path of interest through the magnet. Integrators digitize and integrate the voltage induced in the coil, which corresponds to the magnetic flux linked to the coil. An optical encoder is used to generate a trigger on a spatial basis for the integrators.

Mathematically convolution is used to describe the link between the measured flux and the wanted field. A couple of approaches are presented to solve this inverse convolution problem. After analyzing the approaches in spatial as well as in frequency domain, it shows that a spline basis is the best approach. We used the measurement results to extract the pseudo multipole coefficients, which are a 3D extension of the field harmonics.

Kurzzusammenfassung

Das Ziel dieser Arbeit ist es ein neues Messgerät vorzustellen, welches zur Magnetfeldmessung von Beschleunigermagneten dient. Es wird eine detailierte Beschreibung des Translating-Coil Magnetometers als Modell sowie als System gezeigt.

Messungen wurden an einem Referenzdipol am CERN ausgeführt. Es werdendie Ergebnisse von der metrologischen Charakterisierungskampange, gemeinsam mit einer Erläuterung des Kalibrierungsprozesses, der die Herleitung von systematischen Korrekturfaktoren inkludiert, präsentiert. Die Untersuchungen zeigen, dass das Translating-Coil Magnetometer ein vielversprechendes Messgerät für magnetische Messungen ist.

Als zugrunde liegendes Prinzip, wird auf das Farady Gesetz zurückgegriffen. Es wird angewendet auf eine Spule die sich entlang eines definierten Pfades durch den Magneten bewegt. Integratoren digitalisieren und integrieren die in der Spule induzierte Spannung, welche dem magnetischen Fluß durch die Spule entspricht. Ein optischer Encoder wird verwendet um ein Triggersignal abhängig von der Position für die Integratoren zu erzeugen.

Mathematisch betrachtet wird eine Faltung verwendet um den Zusammenhang zwischen gemessenem Fluss und gesuchtem Feld zu beschreiben. Einige Ansätze werden präsentiert um das inverse Faltungsproblem zu lösen. Nach der Analyse im Ortsraum als auch Frequenzraum, zeigt sich, dass eine Spline Basis am besten geeignet ist. Die Messergebnisse werden verwendet um die pseudo-multipole Koeffizienten zu berechnen, welche eine 3D Erweiterung der Feldharmonischen darstellen.

Contents

List of Figures

List of Tables

1 Introduction To Magnetic Measurement

Particle accelerator need magnets for steering, focusing and other corrections, in order to keep particle beams inside the beam pipe. Nowadays, magnets are designed, using powerful computational tools. They are an important tool, when it comes to optimization. Crucial magnet properties like field strength, field shape and homogeneity are affected by many non-calculable influences. This can be the magnet geometry, due to manufacturing tolerances, as well as properties of the magnetic materials. This raises the need of measuring the field inside the aperture of such magnets [1]. There are a couple of well established magnetic field measurement methods, which shall be presented in a brief way on the following pages. Further we lay out the motivation for a new measurement device.

1.1 Stretched wire

This measurement method is based on a wire stretched through the aperture of a magnet. A loop is formed by this thin wire and a return wire outside of the magnet. The stretched wire is displaced precisely by two displacement stages. The flux in the loop changes by moving the wire and a voltage can be measured [2].

When the aperture is free of any conductive and permeable material, the theoretical description comes down to the following. The measured voltage is related to the change in magnetic flux by the Faraday law $U(\partial\mathscr{A}) = \mathrm{d}\Phi/\mathrm{d}t$. A line element of the wire $\mathrm{d}\mathbf{r}$ that moves during the time interval $\mathrm{d}t$ covers a surface equal to $\mathrm{d}\mathbf{a} = (\mathbf{v} \times \mathrm{d}\mathbf{r})\,\mathrm{d}t$ [3].

Introducing the electromotive force, that is the integral of $\mathbf{v} \times \mathbf{B}$ along the wire,

we express the time derivative of the flux as

$$\int_{\partial\mathscr{A}} (\mathbf{v}\times\mathbf{B})\cdot \mathrm{d}\mathbf{r} = -\int_{\partial\mathscr{A}} \mathbf{B}\cdot(\mathbf{v}\times \mathrm{d}\mathbf{r}) = -\int_{\partial\mathscr{A}} \frac{\mathrm{d}}{\mathrm{d}t}(\mathbf{B}\cdot \mathrm{d}\mathbf{a}) = -\frac{\mathrm{d}\Phi}{\mathrm{d}t}. \quad (1.1)$$

This voltage is measured on two terminals with an integrator. The input resistance of the integrator needs to be high enough in respect to the wire resistance, in order to correctly measure the flux. We assume the wire is long enough so the stages, including the connectors, instruments and other components, are outside of the field region. This reduces the complexity of the system, thereby the induced voltage is proportional to the field integral times the velocity. The integrated voltage is then proportional to the flux which got intercepted by the surface covered by the movement of the wire [3].

Assuming the system is used in a perfect dipole, so $\mathbf{B} = B_\mathrm{y}\mathbf{e}_y$, and the wire is displaced in x-direction only, the integrated voltage gives

$$\Phi = \int_0^L \int_{x_1}^{x_2} B_\mathrm{y}\mathrm{d}x\mathrm{d}z = (x_2 - x_1)I(B_\mathrm{y}), \quad (1.2)$$

where $I(B_\mathrm{y})$ is the field integral of B_y [3].

A simple consideration leads to the idea to measure the direction of a dipole. This can be done by searching for a displacement direction in the xy-plane where the integrated flux becomes a minimum. Commonly an accuracy of 0.1 mrad is reachable [4].

With further considerations the system is able to measure alignment parameters for quadrupoles, such as the magnetic axis, field direction and the magnetic field strength. The setup can be used with other techniques allowing to measure for example an AC field as well [2][4].

1.2 Rotating coil

Inside the aperture of accelerator magnets the field can be described by field harmonics, as long as there is no conductive or permeable material inside the aperture. The field harmonics are a result of the generalized solution of the Laplace equation. For a compendious explanation of rotating coils, we limit the calculations to 2D fields on circular coordinates. This limitation follows

practical structural conditions, where rotating coils usually cover the entire field over z. The field components are then denoted with the field harmonics A_n and B_n by

$$B_r(r,\phi) = \sum_{n=1}^{\infty} \left(\frac{r}{r_0}\right)^{n-1} \left(B_n(r_0)\sin(n\phi) + A_n(r_0)\cos(n\phi)\right) \tag{1.3}$$

and

$$B_\phi(r,\phi) = \sum_{n=1}^{\infty} \left(\frac{r}{r_0}\right)^{n-1} \left(B_n(r_0)\cos(n\phi) - A_n(r_0)\sin(n\phi)\right). \tag{1.4}$$

In order to obtain the field harmonics by means of measurement, a rotating coil can be used [5].

The core element of a rotating coil is a typically long loop of wire placed parallel to a rotational axis, which is rotated in the magnetic field and therefore has an induced voltage on the terminals of the loop. This voltage is proportional to the angular dependence of the field. The generated signal can be used to determine the coefficients A_n and B_n of the equations 1.3 and 1.4. Typically one of two main types is used, either a radial or a tangential coil. For a radial coil, the loop of wire lies in one radial plane of a cylinder. Such a coil is sensitive to the azimuth field component B_ϕ. On the other hand, there is the tangential coil which is sensitive to the radial field component B_r. It is arranged perpendicular to the radial plane. Of course, a real world coil is neither a perfect radial nor a perfect tangential one [6].

In order to find field harmonics from a measurement, a relation between flux and flux density is needed. This relation now depends on the geometry. For the radial coil we can link the flux to B_ϕ with

$$\Phi(t) = Nl \int_{r_1}^{r_2} B_\phi(r,\phi)\,\mathrm{d}r, \tag{1.5}$$

with N, l, r_1 and r_2 being the geometric coil parameters, number of windings, coil length, inner radius and outer radius. Together with the relation 1.4 the integral can be solved

$$\Phi(t) = \sum_{n=1}^{\infty} S_n^{\mathrm{rad}} \cdot \left[B_n(r_0)\cos(n\omega t + n\Theta) - A_n(r_0)\sin(n\omega t + n\Theta)\right], \tag{1.6}$$

where

$$S_n^{\text{rad}} := \frac{2Nlr_0}{n}\left[\left(\frac{r_2}{r_0}\right)^n - \left(\frac{r_1}{r_0}\right)^n\right] \tag{1.7}$$

are the coil sensitivity factors that depend on the coil geometry [5].

Imperfections in the real world coils change those sensitivity factors. In order to cancel out the effect of some of those imperfections, multiple coils are typically bucked. As several coils are placed on a single rotating structure, it is possible to cancel out some of the effects [6].

1.3 Fluxmeter

While the methods presented above are used in static magnetic fields and induce a voltage by changing the flux through mechanical movement, the fluxmeter has no moving parts. Typically "fluxmeter" is referred to a fixed coil in a dynamic magnetic field. A fixed coil measurement only provides a relative flux change. For an absolute measurement, the starting field would need to be known. For certain relative measurements the starting value can be ignored [7].

The measurement signal mainly depends on the coil's surface and the rate at which the field changes. This gives some further limitations to this method, when the ramp rate of magnets is limited, as well as the available space for the coils [7].

In recent years coils can be manufactured in PCB technology. The coils were designed to cover the theoretical path of a particle through the dipole. This resulted in a curved coil. By arranging multiple coils on a single PCB next to each other, a convenient way was accomplished to measure the integral field homogeneity [8].

1.4 Super-FRS

GSI in Darmstadt, Germany has a new research facility FAIR that is currently under construction. A main part of FAIR is the two-stage in-flight separator Super-FRS. It gets a beam from the SIS100 accelerator. Rare isotopes will be produced by hitting a target with the primary beam. Those will then get

spatially separated within the separators of the Super-FRS. This will allow to study very short-lived nuclei of rare-isotopes of all elements up to uranium [9].

As this machine has a high momentum acceptance ($\pm 2.5\,\%$) and a large angular acceptance ($\phi_x = \pm 40\,\text{mrad}, \phi_y = \pm 20\,\text{mrad}$), it therefore requires the magnets to have a large aperture. To achieve this, the magnets were chosen to have a superferric design. While the coils are superconducting, the field is mainly shaped by an iron yoke. For the entire Super-FRS a variety of magnets are needed, in total 24 dipole magnets and 31 so-called multiplets composed of quadrupoles and higher-order corrector magnets in different configurations. As for the dipole magnets there are two types, both are H-type magnets with racetrack coils. The main parameters for the dipoles are summarized in Table 1.1 [10][11].

		Type 2	Type 3
Number of magnets		3	21
Dipole field	T	0.15–1.6	0.15–1.6
Bending angle	°	12.5	9.75
Curvature radius	m	12.5	12.5
Effective straight length	m	2.4	2.13
Good field region	mm	±190	±190
Pole gap height	mm	170	170
Integral field quality	relative	$\pm 3 \times 10^{-4}$	$\pm 3 \times 10^{-4}$

Table 1.1: Main parameters for the dipole magnets of the Super-FRS. Data taken from [11].

1.5 Motivation for the translating-coil magnetometer

The design of the dipole magnets for Super-FRS raises some specific requirements for the magnetic field measurement. One of the challenges is the size of the good field region, with a total region of 400 mm × 140 mm. Further, as those magnets have a large fringe-field, the longitudinal field profile must be measured. The requirements for the standard measurement program are to measure at three different longitudinal sections and cover the field over 3.5 m.

The fringe-fields are significantly effected by the excitation current level and the excitation history. For this reason, the measurement program also foresees to measure at different current plateaus. An additional challenge is that the magnets are foreseen to have a slow ramp rate of 0.016 T/s [12].

The need for a longitudinal field profile eliminates the possibility of using a stretched wire system, see Sec. 1.1. A classical fluxmeter might be able to measure in three longitudinal parts, but it requires a large amount of coil windings, because of the slow ramp rate. It is challenging to obtain a good signal-to-noise ratio while having a feasible amount of windings [12]. Another choice would be the magnetic mapper as in [13]. This device needs a long time for a complete map and is therefore excluded from the possible devices.

A recently presented device in [12] consists of a coil array that is slid through the magnet, parallel to the magnet axis. It intercepts the B_y component of the magnetic flux density. First measurements with a prototype showed promising results and further motivated to design and build an elaborated device for the measurement series [12]. We refer to it as translating-coil magnetometer, but to allow an easy reading we use translating fluxmeter within the running text of this work.

Additionally, there is scientific interest as the translating fluxmeter can contribute for a better understanding of the field distribution of accelerator magnets, due to the longitudinal resolution.

2 The Translating-Coil Magnetometer

The main part of the translating fluxmeter is a sliding carriage that holds a coil array and an optical encoder. This carriage slides on two rails, which are fixed to a main plate. The sliding is enabled by a stepper motor that drives the carriage via a pulley and a strained wire. Along the entire stroke there is an encoder strip mounted to the main plate. Together with the encoder on the carriage a movement can be detected.

The system is intended to move along the magnetic axis of the magnet and intercept the B_y component of the magnet's field. As the system is only capable of measuring flux change, an absolute measurement requires the flux at the starting position to be known. This can be achieved by starting far outside of the magnet's field, so the flux is low enough to be neglected. Another option is to measure the field at the starting position with a hall sensor.

The voltage, which is induced by the change of the flux linked to the coil, depends on the field profile and as well on the velocity of the carriage. The encoders duty is to remove the dependence of the velocity by supplying an integrator with triggers. Those triggers are equally spaced. Mathematically this is a reparametrization of the signal with respect to the arc-length of the trajectory. Some further processing on the measured signal is needed to obtain the demanded B_y.

This design was presented in [12] together with results from the prototype. Grounded on these experiences a new version was designed at CERN. See Fig. 2.1 for the model of the new design. Among other changes, it is adapted to the size requirements of the Super-FRS dipole magnets.

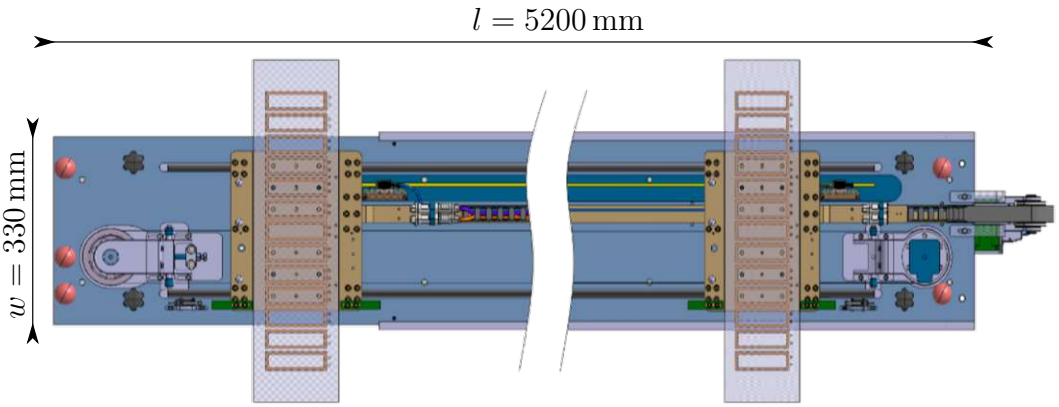

Figure 2.1: The new design of the translating fluxmeter respects the experiences gathered from the prototype.

2.1 Theoretical modeling

The sensing element of the translating fluxmeter is a coil. The flux linked to such a coil can be described as

$$\Phi\left(\mathscr{A}\right) = \int_{\mathscr{A}} \mathbf{B} \cdot \mathrm{d}\mathbf{a}. \tag{2.1}$$

Whereas in our case the surface $\mathscr{A}$ is associated to the coil, and the field $\mathbf{B}$ describes the flux density of the field to be measured.

According to the Farady's law, a change of flux in time through a defined surface, gives a voltage along the rim of the surface $U\left(\partial\mathscr{A}\right) = -\mathrm{d}\Phi/\mathrm{d}t$. So the time derivative of Eqn. 2.1 gives

$$U\left(\partial\mathscr{A}\right) = -\frac{\mathrm{d}}{\mathrm{d}t}\int_{\mathscr{A}} \mathbf{B} \cdot \mathrm{d}\mathbf{a}. \tag{2.2}$$

For now we assume that the coil has one open terminal. This allows to confine the voltage $U\left(\partial\mathscr{A}\right)$ to a voltage u at the terminal, so $U\left(\partial\mathscr{A}\right) = u$.

In order to have a closer look at the components that influence u we apply the Leibniz integral rule to Eqn. 2.2. This gives us

$$u = \int_{\mathscr{A}} \left(\underbrace{\frac{\partial \mathbf{B}}{\partial t}}_{(1)} + \underbrace{\mathbf{v}\,\mathrm{div}\,\mathbf{B}}_{(2)} \right) \cdot \mathrm{d}\mathbf{a} - \int_{\partial\mathscr{A}} \left(\mathbf{v} \times \mathbf{B}\right) \cdot \mathrm{d}\mathbf{r}; \tag{2.3}$$

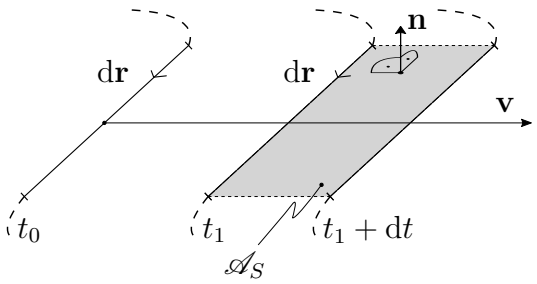

Figure 2.2: A moving line element spans an area $\mathscr{A}_s$ and defines a normal vector $\mathbf{n} = \mathrm{d}\mathbf{r} \times \mathbf{v}$.

as shown in [14] together with further explanations. In our case we assume a static magnetic field so the first term (1) becomes zero. Also we assume to have a source free volume in the magnet's aperture. Therefore the second term (2) becomes zero as well. When the integrand is zero the entire integral becomes zero, so we are left with

$$u = -\int_{\partial\mathscr{A}} (\mathbf{v} \times \mathbf{B}) \cdot \mathrm{d}\mathbf{r}. \tag{2.4}$$

For studying the equation above, we can rearrange the integrand $(\mathbf{v} \times \mathbf{B}) \cdot \mathrm{d}\mathbf{r} = (\mathrm{d}\mathbf{r} \times \mathbf{v}) \cdot \mathbf{B}$. We write the velocity as $\mathbf{v} = \mathrm{d}\mathbf{s}/\mathrm{d}t$. Then it becomes comprehensible that $|\mathrm{d}\mathbf{r} \times \mathbf{v}|$ describes the surface element $\mathscr{A}_s$ spanned by the line element $\mathrm{d}\mathbf{r}$ moved along $\mathrm{d}\mathbf{s}$. The direction of the cross product gives the normal vector $\mathbf{n}$ on this surface element. Therefore the dot product picks out the component of $\mathbf{B}$ which stands normal to the surface element, see Fig. 2.2.

In order to digitize the voltage from the coil terminals we use so-called fast digital integrators (FDI) in our setup. Those are integrators that output a value whenever a trigger occurs, see Sec. 2.2.2. By integrating they give us the flux between two trigger points $\Delta\Phi$, when we feed it with the voltage from Eqn. 2.4. This process can be modeled by

$$\Delta\Phi_n = \int_{t_{n-1}(s_{n-1})}^{t_n(s_n)} u\mathrm{d}t\,, \qquad n \in \{1, 2, \ldots, z_{max}/\Delta z\}\,. \tag{2.5}$$

The trigger signal is generated by the encoder mounted to the sliding carriage. It generates a trigger after a certain constant distance Δz (assuming there is no change in direction). The timing of the trigger depends on the velocity of

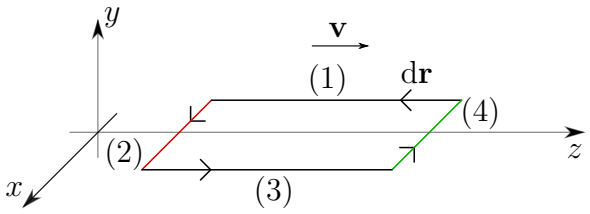

Figure 2.3: With the evaluation of the cross product from Eqn. 2.6, we see that part (2) has a negative (red) contribution while part (4) has a positive (green) contribution. Parts (anti-)parallel to $\mathbf{v}$ don't contribute.

the carriage. By generating a trigger on a spatial base instead of a time base, removes the dependency of the measured signal on the velocity, as shown in Eqn. 2.6. This principle is referred as reparametrization [15]

$$\begin{aligned}
\Delta\Phi_n &= \int_{t_{n-1}(s_{n-1})}^{t_n(s_n)} u\,\mathrm{d}t \\
&= \int_{t_{n-1}(s_{n-1})}^{t_n(s_n)} \int_{\partial\mathscr{A}} (\mathbf{v}\times\mathbf{B})\,\mathrm{d}\mathbf{r}\mathrm{d}t \\
&= \int_{t_{n-1}(s_{n-1})}^{t_n(s_n)} \int_{\partial\mathscr{A}} -\mathbf{B}\cdot(\mathbf{v}\times\mathrm{d}\mathbf{r})\,\mathrm{d}t \\
&= \int_{t_{n-1}(s_{n-1})}^{t_n(s_n)} \int_{\partial\mathscr{A}} -\mathbf{B}\cdot(\underbrace{\mathbf{v}\mathrm{d}t}_{\mathrm{d}\mathbf{s}=\mathbf{v}\mathrm{d}t}\times\mathrm{d}\mathbf{r}) \\
&= \int_{s_{n-1}}^{s_n} \int_{\partial\mathscr{A}} -\mathbf{B}\cdot(\mathrm{d}\mathbf{s}\times\mathrm{d}\mathbf{r})\,. \qquad (2.6)
\end{aligned}$$

To simplify further considerations we assume that an idealized rectangular coil slides along the z-axis and its position is described by z. Also, the coil lies in the xz-plane, so it only intercepts the B_y component of the magnetic field. In order to analyze Eqn. 2.6, we can seperate the rim of the coil into 4 lines with a consistent direction. Referring to Fig. 2.3, the two lines (1) and (3) do not contribute anything to the signal because they move parallel to the moving direction $\mathrm{d}\mathbf{s}$, while the parts (2) and (4) are perpendicular to the moving direction. Parts (2) and (4) do contribute but they do so with different signs.

In order to get the trend of the flux along z, the delta fluxes are summed up

$$\Phi_n = \Phi_0 + \sum_{n'=1}^{n} \Delta\Phi_{n'}, \tag{2.7}$$

where Φ_0 is the flux at the starting position. We denote the flux $\Phi[n]$ as Φ_n and link the index to the longitudinal position $z = n\Delta z$. [1]

Flux is confined to a geometric structure, this prevents a comparison between different measurement methods and has only limited utility. For that reason we want to link the flux to a flux density. A first naive approach assigns the flux at each position a flux density proportional to the coil's surface A_C,

$$B_\mathrm{y}(z) = \frac{\Phi_n}{A_\mathrm{C}}. \tag{2.8}$$

This turns out to be a simplified version from Eqn. 2.1. A correct value is only retrieved when the flux density inside the entire coil is constant at each step. For a more elaborated description we use Eqn. 2.1 and apply our assumptions of an idealized coil, so we get

$$\Phi(z) = A'_\mathrm{C} \int_{z-\frac{L_s}{2}}^{z+\frac{L_s}{2}} \overline{B}_\mathrm{y}(z')\,\mathrm{d}z', \tag{2.9}$$

where $\overline{B}_\mathrm{y}$ is the y-component of the flux density that only depends on the position in z averaged over the coil width W_s,

$$\overline{B}_\mathrm{y}(z) = \frac{1}{W_s} \int_{-W_s/2}^{W_s/2} \mathbf{B}(x, y = const., z) \cdot \mathbf{e}_\mathrm{y}\mathrm{d}x. \tag{2.10}$$

This is valid for a (imaginary) coil, where the extension of the windings can be considered to be small enough. The effective surface of the coil A_C is a product of the coil's length L_s, the coil's width W_s and the number of turns. Whereas the length-related coil surface is $A'_\mathrm{C} = A_\mathrm{C}/L_s$.

From Eqn. 2.9, we remove the variable integration limits and instead introduce a sensitivity function $s(z)$ that describes the coil's length dependent surface,

$$s(z) = \begin{cases} A'_\mathrm{C}, & -\frac{L_s}{2} < z < \frac{L_s}{2} \\ 0, & \text{else} \end{cases}. \tag{2.11}$$

[1] Magnetic flux is a global quantity confined to a surface. With Φ_n we understand the flux confined to the coil placed at the position $n\Delta z$.

This sensitivity function can be adapted to real-world coils, but for the sake of simplicity we stick with the hard-edge model here. Anyway, the surface under the sensitivity function shall be equal to the effective surface of the coil $A_\mathrm{C} = \int s(z)\mathrm{d}z$. Now we can write

$$\Phi(z) = \int_{-\infty}^{\infty} \overline{B}_\mathrm{y}(z')\, s(z'-z)\mathrm{d}z'. \tag{2.12}$$

By flipping the sensitivity function we can see that this is a convolution between the flux density $\overline{B}_\mathrm{y}$ and the flipped sensitivity function $s(z)$. Let $\widehat{F}$ be the flipping operator, thus $\widehat{F}f(t) = f(-t)$. Now we can write for the flux along z

$$\Phi(z) = \left(\overline{B}_\mathrm{y} * \widehat{F}s\right)(z). \tag{2.13}$$

It can be understood by picturing the coil sliding through the magnetic field. While a convolution flips one function and slides it over the other function, we don't flip the coil (ergo the coil's sensitivity function). That is why mathematically we need to flip the sensitivity function to be able to describe the problem as a convolution [2]. Following the naming of imaging systems we can call $\widehat{F}s(z)$ point spread function $PSF(z) = \widehat{F}s(z)$.

We need to solve this inverse problem in order to find $\overline{B}_\mathrm{y}$ for the measured $\Phi(z)$. For the inverse problem the kernel PSF plays an essential role. So it is important to precisely model it and also choose a well thought-out design, see Chapter 5.

We show that for calculating the integral field $B_\mathrm{I} = \int \overline{B}_\mathrm{y}(z)\mathrm{d}z$ we can follow the naive approach from Eqn. 2.8 [15]. We start by integrating over Eqn. 2.12

$$\int_{-\infty}^{\infty} \Phi(z)\,\mathrm{d}z = \int_{-\infty}^{\infty}\int_{-\infty}^{\infty} \overline{B}_\mathrm{y}(z')\, s(z'-z)\mathrm{d}z'\mathrm{d}z. \tag{2.14}$$

According to Fubini's theorem we can switch the order of integration. $\overline{B}_\mathrm{y}(z')$ depends only on z' and therefore we can extract it from the inner integration,

$$\int_{-\infty}^{\infty} \Phi(z)\,\mathrm{d}z = \int_{-\infty}^{\infty} \overline{B}_\mathrm{y}(z') \int_{-\infty}^{\infty} s(z'-z)\mathrm{d}z\mathrm{d}z'. \tag{2.15}$$

[2] We can also interpret it as cross-correlation $\Phi(z) = \left(\overline{B}_\mathrm{y} \star s\right)(z)$

By definition the integral over the sensitivity function is equal to the effective coil surface and independent from any shift. Therefore we are left with

$$\int_{-\infty}^{\infty} \Phi(z)\,\mathrm{d}z = A_\mathrm{C} \int_{-\infty}^{\infty} \overline{B}_\mathrm{y}(z')\,\mathrm{d}z' \quad \Rightarrow \quad B_\mathrm{I} = \int_{-\infty}^{\infty} \frac{\Phi(z)}{A_\mathrm{C}}\mathrm{d}z. \tag{2.16}$$

When the field integral of interest doesn't span the entire stroke, we need to adjust the limits of the outer integral in Eqn. 2.14. So we cannot calculate the field integral only for a part of the full stroke when we use the naive deconvolution approach.

2.2 System design

To describe the entire system we split it in three subsystems, the mechanical, the electronic and the software subsystem. A simple schematic for the system design of the translating fluxmeter is shown in Fig. 2.4, the systems are not shown to their full extend here. Refer to the more detailed schematics in the corresponding paragraphs. Only when all subsystems work well together, the measurements can achieve a high quality.

2.2.1 Mechanical subsystem

The fundamental idea of this measurement method is based on moving a coil. Therefore it is obvious that a well defined motion is a crucial part of the system. The mechanics define the path of the carriage transporting the coil. We need the path to be as straight as possible and robust to deformations by external forces, including gravity. As a counterpart acts the requirement to have a low profile. A high structure would prevent the measurement of magnets with a tight aperture.

The sliding mechanism effects the smoothness of the movement. Inherent to sliding is the conflict that for sliding a certain amount of freedom is needed, while this freedom prevents a well defined path. Other tasks of the mechanical system are to linearly move the carriage by a motor and support the encoder system.

Additional to those challenges add the general requirements for a magnetic

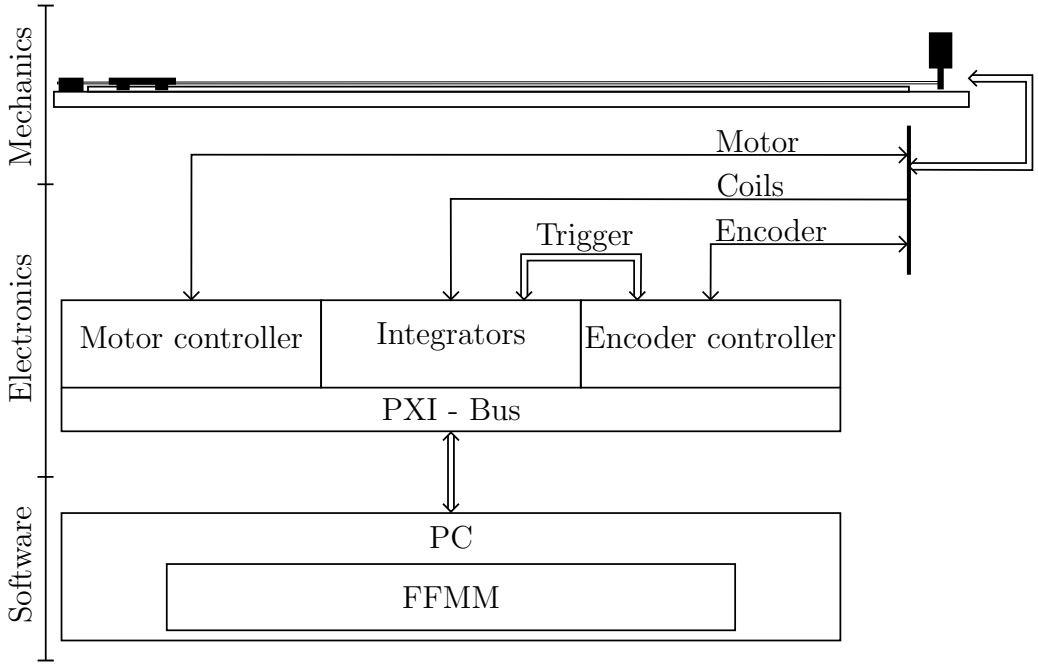

Figure 2.4: The system can be split in three subsystems, a mechanical one, an electrical one and a software one. More detailed diagrams for the individual subsystems are shown further down.

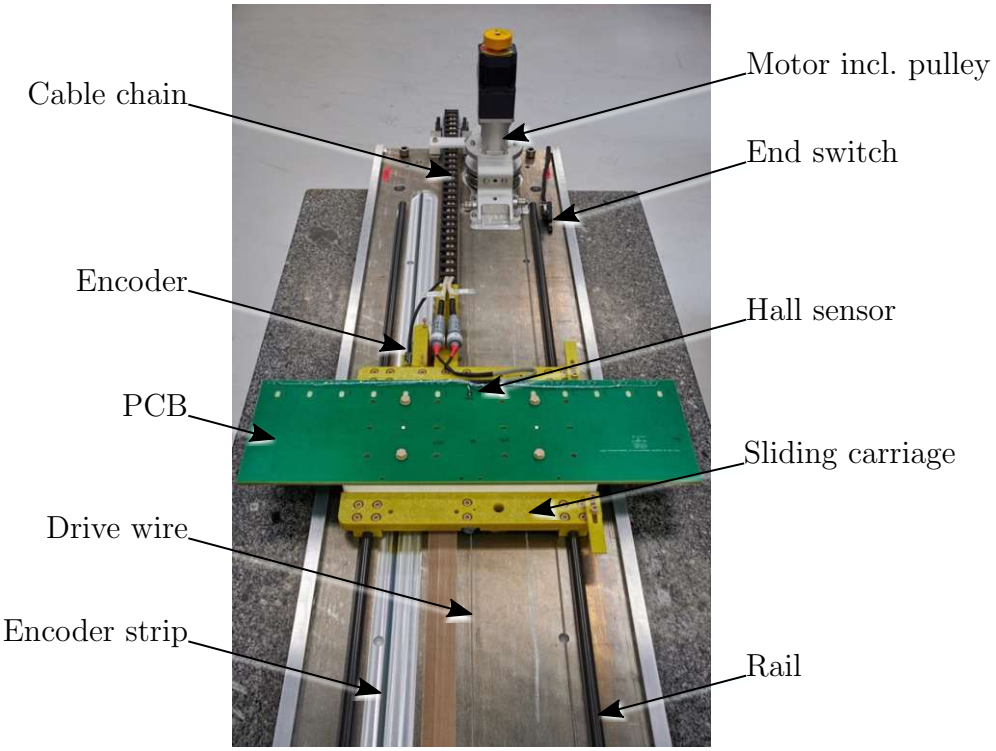

Figure 2.5: Picture of the translating fluxmeter with the most essential components labeled.

measurement system, especially no moving conductive material and only non-magnetic materials inside the magnetic field.

To overcome those challenges the main part is formed by an aluminum plate, with 5200 mm × 330 mm × 15 mm. The main plate together with the most crucial parts are explained in the further paragraphs and shown in Fig. 2.5. Onto this main-plate two rails are mounted in a distance of 220 mm to each other. The carriage is equipped with the fitting slide shoe. Since the carriage together with the slide shoes is a stiff structure, the rails need to be placed nearly perfectly parallel to each other to assure a smooth sliding. The rails are manufactured by an external company, with a tolerance h8 on 12 mm diameter.

In order to translate the carriage, a stepper motor is in use. It is mounted on one side together with a pulley. The pulley and a driving wire transmit the force to the carriage. Together with the gear box the motor has a minimal resolution of

0.18 deg in the full-step setting. Combined with the pulley, which has a diameter of 90 mm, this results in a theoretical minimal translation distance of 0.14 mm. Nevertheless this can be reduced by using microsteps. It is obvious that the driving wire needs to be under tension to assure an immediate transmission. The second pulley on the other side of the motor is supplied with a structure that allows to tension the wire.

As shown in Sec. 2.1 we want the trigger for the integrators to occur after a well defined distance. To achieve this, we use an optical encoder. An encoder head is mounted on the carriage while an encoder strip is glued to the main-plate, right below the encoder head. In order to assure a trouble-free operation, the alignment of the head needs to stay within strict limits as given in Table 2.1. Those limits cover the distance to the strip as well as an angular misalignment in all directions. To be able to stay within those limits, it is required to have a stiff but adjustable mounting structure for the head. See Fig. 2.6 for the mounting structure used on the translating fluxmeter.

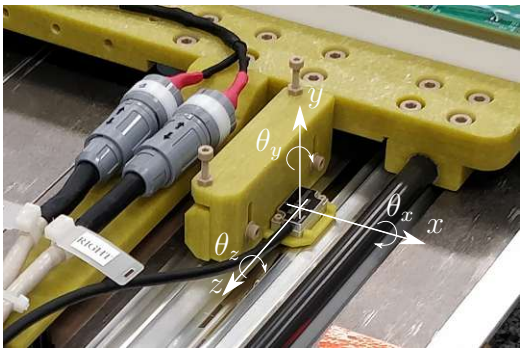

Figure 2.6: Four screws are used to precisely align the encoder head above the strip.

Axis		Alignment tolerances
x	mm	± 0.2
y	mm	± 0.15
z		Direction of motion
θ_x	°	± 1.0
θ_y	°	± 2.0
θ_z	°	± 1.0

Table 2.1: Specified tolerances for the alignment of the encoder head to its reference position after [16]. The frame is given in Fig. 2.6.

2.2.2 Electronic subsystem

We use complex control electronics and a precise measurement hardware for the translating fluxmeter. The majority of the system is composed of components that are already in use at other magnetic measurement systems at CERN, such as the fast digital integrator.

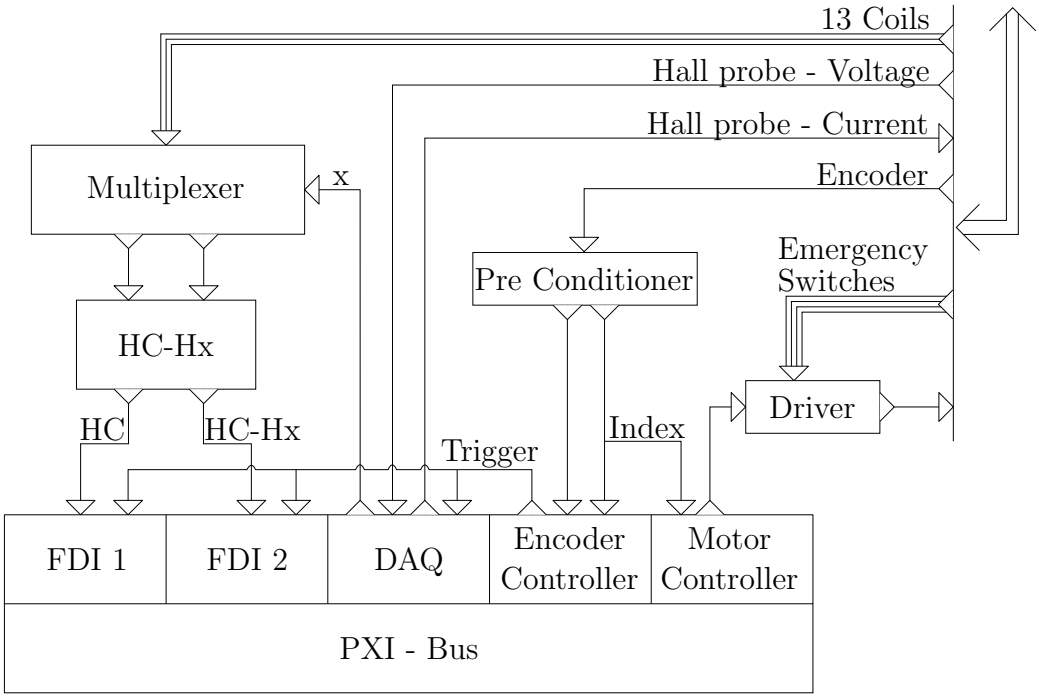

Figure 2.7: The central part of the electronic system is the acquisition with the integrators including the trigger generation. HC... Central coil; HX... Coil X; FDI... Integrator; DAQ... Data acquisition; PXI... Backbone for measurement systems

Fast digital integrator The fast digital integrator (FDI) was developed to keep up with the demands of magnetic measurement systems. It is designed to integrate the applied voltage, typically generated with a fluxmeter, between two triggers generated by an encoder together with an encoder board. The input is equipped with an programmable gain amplifier, which has an auto-calibration capability. The amplified signal is sampled with a high-quality successive approximation register ADC. The signal processing happens on a DSP together with an FPGA, which gives a high processing power and large I/O capabilities. The ADC works with a maximum sampling rate of 500 kS/s. Based on the Nyquist theorem a maximum bandwidth of 125 kHz is derived. The integration happens with the internal clock for the ADC, while the external trigger makes the DSP release a magnetic flux sample. For the integration, an algorithm based on the trapezoidal rule is implemented. Since the trigger is generated by an external system, it is in general not synchronous with the sampling frequency of the ADC. To reduce uncertainties, the FDI uses a signal reconstruction. The first and last part of the integral is reconstructed using a linear interpolation between the samples of the time-wise closest neighboring samples. In order for this structure to work accurately, the FDI needs a stable time base. This is achieved with an oscillator on a 20 MHz base, which has a low phase noise and a long term stability of ± 0.3 ppm in 1 year [17].

A detailed schematic of the electronic subsystem is shown in Fig. 2.7. It is immediately recognizable that all crucial components are connected to a PXI-Bus. Via this bus system, the components are controlled by a PC, which is connected to this bus as well. As we want a fast acting system, all controllers are configured at first and then wait for trigger signals to do their foreseen jobs.

The system can be further unraveled by splitting it in three minor parts - the acquisition part, the motor part and the encoder part. The encoder is a central piece as it gives the location information to the integrators and also to the motor controller. For the integration a trigger signal for each measurement point is needed. The motor controller on the other hand asks for two pulses. The first pulse has no effect on the motor controller, but the second pulse gives the stop command. So after the second pulse the motor starts to decelerate with the predefined rate. Those two pulses are generated when the encoder head passes an index marker. Those markers are manually glued to the encoder strip. When the encoder head passes an index marker, it outputs a pulse on a separate pin. They are commonly used to define a reference position. In our

system the index markers have the further task to start (first marker) and stop (second marker) the output of the trigger signal for the integrators. Such an index marker is placed manually with great care onto the encoder strip.

The acquisition part consists of integrators, a voltmeter in form of a data acquisition device (DAQ) and a multiplexer. In the current setting the system can measure up to 13 coils and one hall probe. To avoid the need of 13 integrators there is a multiplexer implemented. Together with the multiplexer we measure on one cycle only 2 coils. One of those coils is always the same and is referred as the absolute coil - typically the central one. The second coil can be changed with the multiplexer. To obtain a complete set of data, multiple runs are performed with different coils. The multiplexer also takes over the compensation. So the second output of the multiplexer is the difference between the absolute and the second, the relative, coil. For this kind of measurement two integrators are needed. The system uses the same type of integrators which are in use in other systems, the FDI, see above. For the acquisition of the hall probe signal is the DAQ device PXI-6289 from National Instruments™ in use.

The motor part consists of a controller card connected to the PXI-Bus and a driver for the stepper motor. The driver is equipped with an emergency switch, that cuts the power. Aside from the yellow-red emergency switch the translating fluxmeter is equipped with end switches. In case the motor doesn't stop in time, the carriage hits the switch and thereby stops the motor before crashing into something.

Sensing Element

A central element of the entire measurement system are the coils. It proves to be handy to connect multiple similar coils to a single mechanical structure. A good way is to manufacture a PCB with coils, as it was already done in other projects [8]. The design specification for the board used with the translating fluxmeter consists of 14 layers, each layer has 12 windings per coil. The average dimensions of a coil are 130 mm × 28 mm, that roughly results in an effective surface of 0.61 m^2. There are 13 identical coils placed on the board, distributed evenly with a shift of 38 mm. See Fig. 2.8 for the layout of one layer of a single coil with its dimensions. One can see, that the windings were placed as close to each other as possible, with the idea to have a hard edge model as in Eqn. 2.11.

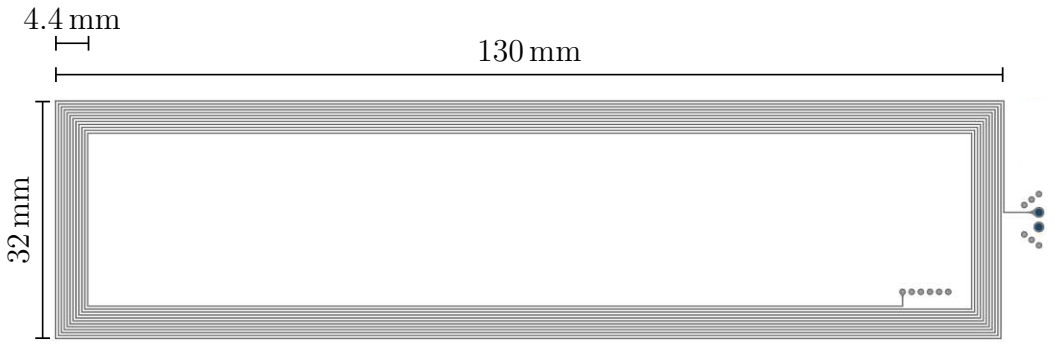

Figure 2.8: This shows the layout of one layer of one coil. The design of this coil is replicated 13 times on the PCB per layer. Vias inside and outside of the coils connect the layers.

We introduce a nomenclature for the coils as follows. Looking at the board from the connection side, we can identify a left and a right side. As the central coil takes a special position, we name it HC. This is connected as the absolute coil. All the other coils in general we name HX, where X can be substituted. We start from outside left, the first coil is H6L, then increasing the number until H1L. Then comes the central coil HC and then we continue the naming with H1R until H6R.

Mechanically the board is equipped with a couple of holes for mounting. Four screws fix it to the trolley and two pins assure a precise positioning. To increase the flexibility there are three sets of those holes. This allows to place the PCB at three different lateral positions, spaced with 38 mm.

2.2.3 Control software

The Flexible Framework for Magnetic Measurements (FFMM) is a software framework that gives test engineers a flexible and reusable environment for software development. It allows to easily control the components of a system, take the acquired data, save it, do preliminary processing and visualize it [3].

The framework offers a group of modules to the test engineer. This allows it to be reusable and easy to use, also without a deep knowledge of the framework itself. A design of the modules in an object-oriented way makes this possible. Combined with an aspect-oriented programming the maintainability is assured.

A group of interfaces and abstract classes gives the framework its flexibility and the possibilities to be extended [3].

Typical measurement procedures gave a certain boundary to the development of this framework. An analysis of typical use cases lead to following structure of a measurement program:

- definition of the measurement components;
- specification of mechanical and electrical connections;
- definition of dynamic parameters;
- component checking;
- configuration of measurement devices;
- description of the measurement procedure;
- preliminary data analysis;
- data saving.

The test engineer implements those steps into a user script using the modules from FFMM. Only necessary configurations shall be available to the user [3].

To give a better understanding of the functional principle of the translating fluxmeter, the following paragraph gives the description of the measurement procedure and preliminary data verification. The preceding points from the list above are implemented consequently. Also is the description limited to give an understanding of the procedure rather than a complete program description.

We introduce a terminology to describe the composition of measurements, which shall be used within this work.

Run	a displacement from one side to the other, can be further characterized with go and return;
Cycle	consists of a go- and a return-run;
Set of cycles	are multiple cycles that belong to one coil;
Measurement	is a complete acquisition of all coils;
Measurement series	are multiple measurements with typically different settings.

As mentioned in Sec. 2.2.2 the system is equipped with a multiplexer. To obtain a full measurement we need to do at least one cylce for each coil. To average out some Gaussian noise we want to have the possibility to do a set of cycles. In the program this depicts as two nested loops. The first loop, iterates through all indicated coils. For each coil the multiplexer is set accordingly. The second

loop starts right after setting the multiplexer, it iterates from 0 to $N-1$, with N being the given number of cycles per coil. Within this loop the process of a single cycle can be sub-classified into eight processes, as shown in the flowchart in Fig. 2.9.

At the end of those eight processes a fault check is performed. This is done by checking the velocity of the carriage over the distance. If outliners are detected we can assume that there was something wrong during one of the runs, since the velocity is assumed to be - in certain limits - constant. A possible cause could be dust on the strip, as this prevents the encoder head to do a proper detection. A fault is handled by simply trying it again, but in case faults appear too often the number of extra repetitions is limited. Anyway, in this case the user should try to eliminate the problem.

The processes involved in one cycle are described in detail in the following paragraph together with their corresponding flowcharts (see Fig. A.1-A.7) in the appendix.

Device settings All devices used in this system are multipurpose devices and have therefore a wide variety of settings. By configuring the devices like the FDIs, the encoder board, the motor controller and the DAQ in a trigger driven way, we ensure that the system reacts in real time. In general we can define two different trigger signals. One from the steps of the encoder, the step-trigger and the index trigger from the index markers. The encoder board receives both trigger signals. Its configuration only outputs the step-trigger after receiving the first index-trigger and stops the output after the second index-trigger. Furthermore the encoder board can divide the step-trigger by a given divisor (2, 4, 8, 16, ...). The acquisition devices FDI and DAQ are now configured to take data on a trigger edge. Buffer settings are done accordingly to the estimated trigger frequency. The motor board is configured with the intended ac- and deceleration rate as well as the target velocity. The deceleration is triggered by the second pulse of the index-trigger. Values that are given by the user as input variables are checked before set. The maximal deceleration stroke is mechanically given by the position of the index marker. If the calculated deceleration distance is not within the margin, the user is asked to enter a new velocity. After giving a valid velocity, the motor controller is configured

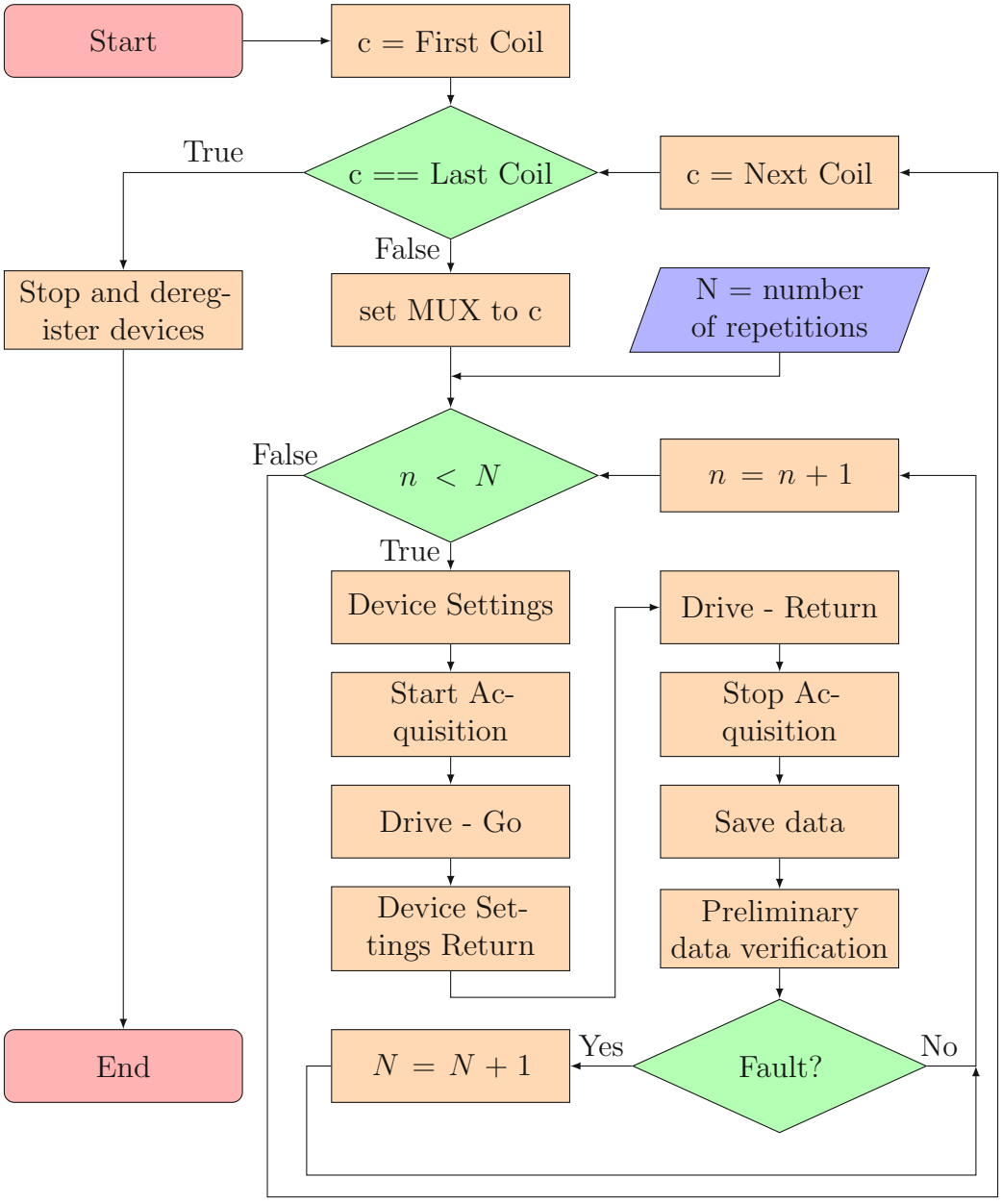

Figure 2.9: The main script is based on two nested loops. The first one iterates the coils and the second one gives redundancy. One cycle can be subclassified into eight processes.

and the program continues.

Start acquisition By supplying the FDIs and DAQ with a software start command, the devices are now ready to receive triggers and take data.

Drive The "Drive" process is called twice per cycle - for the go- and the return-run each once. When all components are ready, the encoder board is activated and the motor is started. The program then waits for the motor to stop.

Device settings return Before starting the return run, the motor controller needs to be reconfigured with a changed direction, as well as the encoder board. This also resets their internal state, so the parts are again ready to receive the index-triggers.

Stop acquisition After a software stop of the FDIs, the registers from the FDIs are checked for an overflow of the ADC. In case of an overflow, the program outputs a warning but doesn't terminate. It is necessary to find the optimum gain for the FDIs empirically as part of the setup. The task of the DAQ is stopped by software without any further check.

Save The acquired data is saved to files. For each cycle we save a new set of files.

Preliminary data verification In order to give the operator a feedback on the measurement, two main plots of the acquired data are shown and a couple of calculations are done. A first insight on the results gives the first plot, which shows the flux over the distance. The second plot shows basically the velocity over the distance. With every measurement point, a time information is stored as well. By taking the difference of the time from point $i+1$ to i, we obtain the delta time. Analyzing the delta time we can detect some basic errors. We can assume that the velocity only changes in a small range. So the program looks for outliers, that deviate from the median within a certain tolerance. Those outliers can appear if the encoders reading was bad, for example because of some dust on the strip. If an outlier was detected a fault status is set to true, which triggers a repetition.

3 System Calibration

Any measurement can be seen as an estimation of an unknown value. A lot of effort is put into the system to get as close as possible with this estimation. Any deviation that is left to the real value we call a measurement error. Of course this error is unknown, but we can estimate a potential magnitude. With this we can name a measurement uncertainty, which gives us an interval of trust [18].

Uncertainty can arise from known and unknown influences. Systematically known influences have a calculable effect on the result. We cannot reduce it by repeating, but it is possible to correct the data for it. This already shows, the importance of a well-known measurement system. Such an effect can appear at any point in the measurement chain and get propagated till the end. The correction needs to take this propagation into consideration. To estimate the sensitivity of the system to certain effects, it is practical to use relative errors [19].

This chapter will focus on the corrections for systematic errors. But every system is affected by many different influences. Often we cannot consider all of them. This leads to a statistical fluctuation of the measurement samples. By repeating the experiment, this error often becomes well modelled with a Gaussian distribution. This can be derived from the central limit theorem for independent variates [18]. A result is given by a mean value with an uncertainty, whereas the uncertainty is the standard deviation of the data [19].

3.1 Systematical impacts and their calibration procedure

During the metrological characterization phase we could identify sources of uncertainty. All of them need to be considered in an appropriate way, to obtain a correct measurement result. A study needs to precede in order to understand the effect and how we can correct for it. After establishing a corrective action, we need to find the amount that we need to correct for. This amount is inherent to the individual setup and needs to be reestablished after a change on the system. Some corrections are derived from each individual cycle.

3.1.1 Coil surface

As it becomes clear in Sec. 2.1 and especially in the Eqns. 2.8 and 2.11, the surface of the coil has a significant impact on the measured flux density. Here it doesn't matter which approach we choose to link the flux with the flux density. An error in the coils effective surface, manifests as a scaling error in the flux density. This asks for a high precision of the coils' surface. Well known measurement techniques like the rotating coil measurement have a very similar issue. Therefore there exist established calibration routines, as described in [7]. The calibration process for the surface happens in a known field with an average B across the coil's area A_C. Within this field the coil gets flipped (turned by 180°). Measuring the signal with an integrator gives an integration process that can be described as

$$-\int_0^t u_c \mathrm{d}t = \Phi - (-\Phi) = 2A_C B. \tag{3.1}$$

In order to reduce the sources of uncertainty, like the integrator drift, see Sec. 3.1.4, the coil is flipped back to its original position [7].

At CERN's magnetic measurement section this process is performed in a reference dipole. The magnetic field inside of the reference dipole is mapped to a high accuracy with a NMR probe (see Sec. 4.6.1). The coils for the translating fluxmeter are small enough to fit entirely into the homogeneous field region of the magnet.

As explained in Sec. 2.2.2, the coil array for the translating fluxmeter is produced with PCB technology. For coils manufactured as PCBs we could

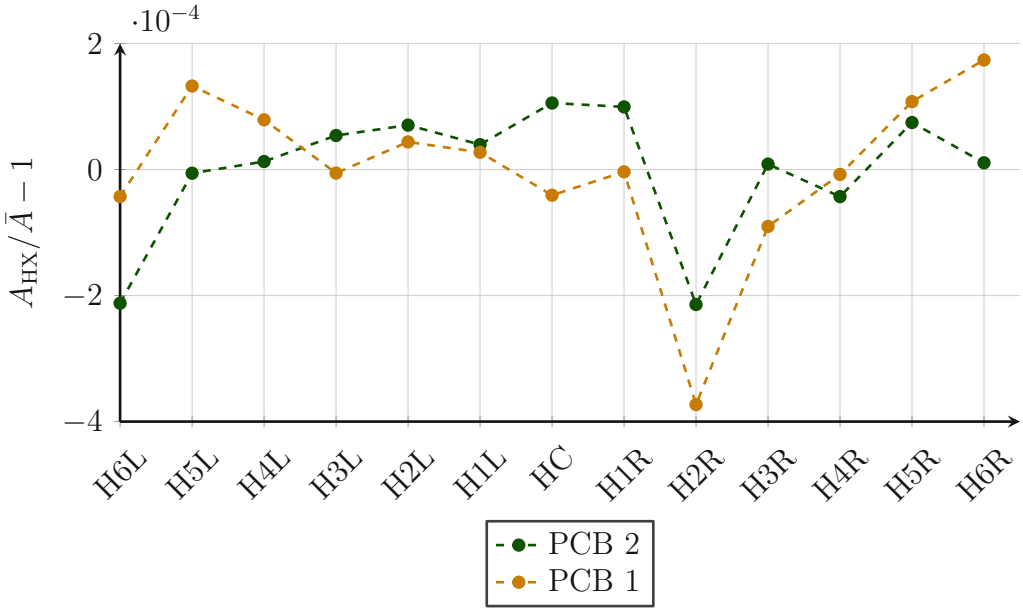

Figure 3.1: The absolute surface calibration campaign for two PCBs is shown as a relative change. The reference value for PCB 1 is $\bar{A} = 0.484\,67\,\mathrm{m}^2$ and for PCB 2 it is $\bar{A} = 0.484\,70\,\mathrm{m}^2$.

forgo the calibration, as we can rely on the designed track position under consideration of the shrinking factor [20]. In order to reveal possible defects in the coils, it is still necessary to do a calibration.

Our PCB consists of 13 coils, where each of them needs to be calibrated separately. In Fig. 3.1 the results from the calibration process for two boards, so in total 26 coils, are shown. Each value is plotted as relative deviation to the mean value of its dedicated board $A_{\mathrm{HX}}/\bar{A} - 1$. The mean value for PCB 1 and PCB 2 are $0.484\,67\,\mathrm{m}^2$ and $0.484\,70\,\mathrm{m}^2$, respectively.

During these studies a mistake in the coils' design was detected. The design has 14 layers foreseen, that should give 14 loops in series. Two of those layers are short circuited unintentionally by design. This leads to only 12 layers that contribute to the voltage at the terminal. The reduced number of layers, reduces the coils surface and further reduces the sensitivity and therefore the accuracy. On a single layer, a coil can wind either from inside to outside or the other way around. Vias usually connect two layers. Per pair of layers we need one via inside and one outside of the coil. The mistake in the wiring is depicted in

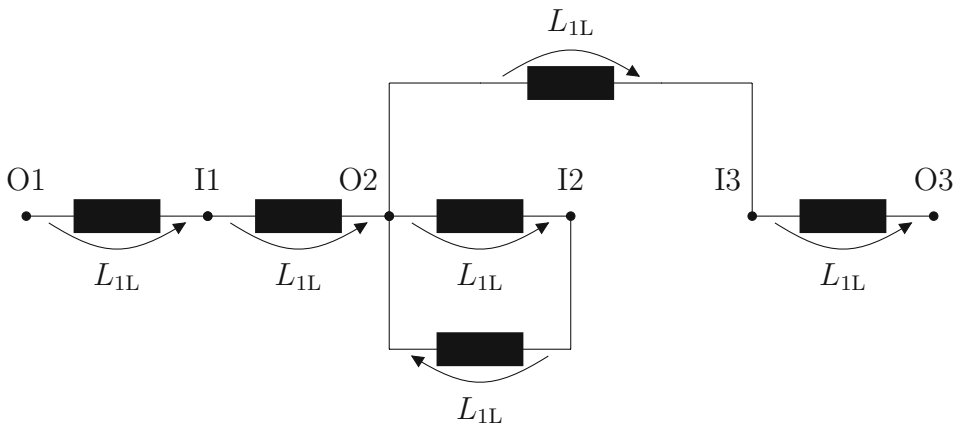

Figure 3.2: The coil of a single layer are modeled as inductance L_{1L} and have each an inside In and an outside connection On. This detail of the circuit model of one PCB coil includes the shorted layers. The arrows indicate the direction of counting the magnetic flux.

Fig. 3.2 as detail of all 14 layers.

Another possibly problematic issue arises from the shorted loops. The Faraday's law still applies to those loops, but since there is no open terminal, the induced voltage drops along the PCB track. This path has a low resistance, we can approximate it by calculating with the specific resistance of copper and take the track dimensions. The induced voltage forces a current to flow in the loop, which again produces a magnetic field that counteracts the inducing field. The phenomenology of this effect is the same as with eddy-currents. An approximate calculation shall show the impact of this issue.

As a first step we approximate the resistance of a single layer. The length of a single layer is around $L = 3.8\,\mathrm{m}$ and the tracks have a width $w = 0.2\,\mathrm{mm}$ and thickness $d = 17.5\,\mu\mathrm{m}$. This gives us a resistance

$$R_{1L} = \frac{L\rho}{wd} = 18\,\Omega \tag{3.2}$$

for one layer. Since the shorted loop consists of two layers, we use $R_{SC} = 35\,\Omega$. In a second step we need an approximation for the voltage change. This we achieve by a rough linearization of the reference dipole's fringe field. We assume that the field goes from 0 T to 1 T within the distance of 5 times the gap size. With a speed of roughly 0.5 m/s we obtain a voltage of 0.11 V. Together with

the resistance of two layers we estimate a current of 3.1 mA in the short circuited loop. The next step is to use this current together with the Biot-Sarvart-Law to calculate computer-aided the field distribution caused by the shorted loop within itself. By integrating the flux density over the loop surface, we obtain the flux linked to itself, approximate 0.9 nV s. Here we also could derive the inductance of such a loop. Now we assume that the mutual inductance of the shorted loop and the rest of the coil is close to one, as they lie directly above each other. This gives us a linked flux through the 12 active layers of 10 nV s. Additionally, by using the inductivity of the shorted loop and its resistance, we can estimate a time constant $\tau \approx 5\,\mu s$, which shows to be small in respect to typical times of the system.

This issue can be addressed by either fixing the design and produce a new PCB or mechanically open the short circuit. The mechanical intervention is a delicate process and doesn't restore the two layers, merely removes the currents.

As stated in the specifications for the measurement campaign a special attention is required for the field homogeneity. For the surface calibration this means that we want to differentiate the surface accuracy in absolute and relative. While the calibration in the reference dipole gives an absolute value for each coil, we can think of a procedure where we measure especially the difference between the coils known as in situ calibration [21]. The big advantage of this procedure is that it can be done with little effort. We need to run 3 measurements and calibrate only one coil in a reference dipole. In the following we describe the realization of the calibration procedure described in [21] adapted for the translating fluxmeter.

We first refine our previous definition for the integral field B_I to

$$B_{\mathrm{I,HX}}\left(\mathscr{S}\right) = \int_{\mathscr{S}} \overline{B}_{\mathrm{y,HX}}(z)\mathrm{d}z \quad , \tag{3.3}$$

whereas $\overline{B}_{\mathrm{y,HX}}(z)$ is $\overline{B}_\mathrm{y}(z)$ for the coil HX. The path $\mathscr{S}$ defines the measurement stroke. For the in situ calibration $\mathscr{S}$ is fixed to the entire measurement stroke between both index markers and is therefore omitted in the following.

We recall that all coils are equally spaced across the PCB, and we have the possibility to place it at three different positions, center, left and right. The shift between those positions is 38 mm and is equal to the shift between the coils.

A measurement with the board on the central position C gives us a set of values for the integrated flux density $B^{\mathrm{C}}_{\mathrm{I,HX}}$ with $X \in \{6\mathrm{L}, 5\mathrm{L}, \ldots, 1\mathrm{L}, \mathrm{C}, 1\mathrm{R}, \ldots, 6\mathrm{R}\}$ - we assume an arbitrary surface for all coils, for example $1\,\mathrm{m}^2$. A second measurement with the board shifted to the left gives us another set of values $B^{\mathrm{L}}_{\mathrm{I,Hx}}$. Since the shift of the board is identical to the distance between the coils, most tracks are measured twice with different coils. For example, the coil H1R saw the exact same field $B^{\mathrm{L}}_{\mathrm{I,H1R}}$ as the coil from H2R saw in the first measurement $B^{\mathrm{C}}_{\mathrm{I,H2R}}$. The ratio between those two results is equal to the ratio of the two surfaces. This can be carried forward for all coils

$$\frac{B^{\mathrm{L}}_{\mathrm{I,H(X-1)}}}{B^{\mathrm{C}}_{\mathrm{I,HX}}} = k^{\mathrm{L}}_{\mathrm{H(X-1),HX}} = \frac{A_{\mathrm{H(X-1)}}}{A_{\mathrm{HX}}}. \tag{3.4}$$

By shifting the board to the negative direction, we can measure a third set of data

$$\frac{B^{\mathrm{R}}_{\mathrm{I,H(X+1)}}}{B^{\mathrm{C}}_{\mathrm{I,HX}}} = k^{\mathrm{R}}_{\mathrm{H(X+1),HX}} = \frac{A_{\mathrm{H(X+1)}}}{A_{\mathrm{HX}}}, \tag{3.5}$$

where we used the notation H(X±1) to identify the neighboring coil of HX.

For each set $k^{\mathrm{L}}_{\mathrm{H(X-1),HX}}$ and $k^{\mathrm{R}}_{\mathrm{H(X+1),HX}}$ we can find the factors between the central coil to any other coil $k^{\mathrm{L}}_{\mathrm{HX,HC}}$ and $k^{\mathrm{R}}_{\mathrm{HX,HC}}$. Because theoretically the factors $k^{\mathrm{R}}_{\mathrm{HX,HC}}$ and $k^{\mathrm{L}}_{\mathrm{HX,HC}}$ should be the same, we calculate an average and can estimate a variance. This gives us the homogeneity profile of the coils' surfaces.

This was done with the installed PCB during the characterization campaign, further explained in Sec. 4.1. In Fig. 3.3 the results are shown in comparison to the results from the absolute calibration. The relative surfaces refer to the surfaces of the central coils $A_{\mathrm{HX}}/A_{\mathrm{HC}} - 1$. The in situ calibration gives a strong deviation on the outer coils. Since the board is much bigger than the magnet's pole, only approx. 5 coils were within the pole. The signal of the outer coils was already rather small and therefore has a rather low significance and introduces errors. We suspect the results to be more precise when the same measurement gets done in a large magnet, where the PCB is entirely in a strong homogeneous field. The error approximation mentioned above, reinforces the low trust in the outer coil calibration.

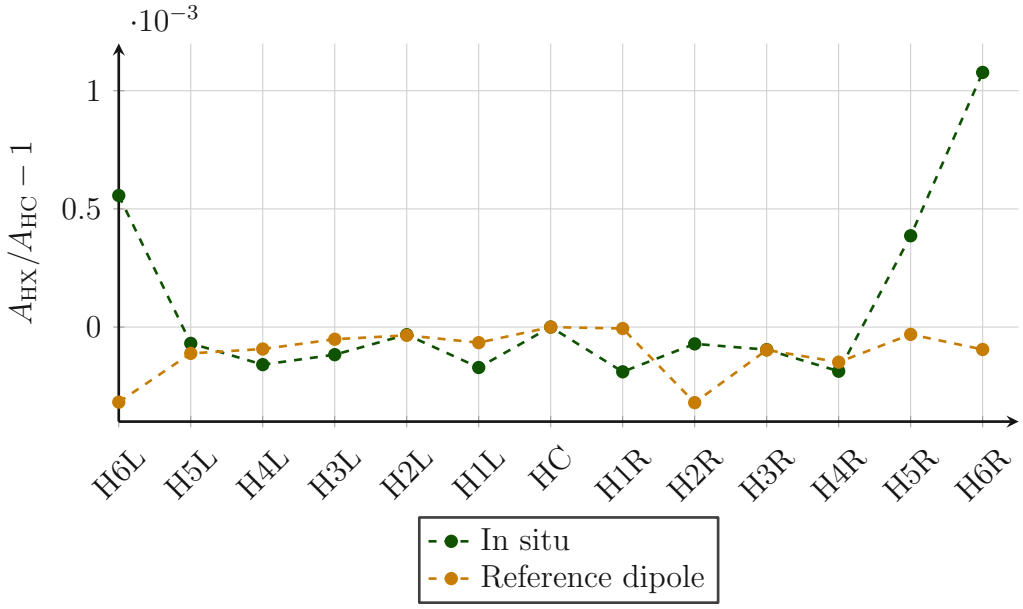

Figure 3.3: The relative surface is shown with the central coil HC as reference. Results from the in situ calibration are compared to an absolute calibration in the reference dipole.

3.1.2 Network compensation

The input resistance of the FDI is finite, also the resistance of the coils is not zero. This raises the need of including a factor to compensate for the voltage divider between the coil and the FDI. We model the input of the FDI with a resistor and an ideal voltmeter measuring the voltage drop on the resistor. Our electrical network consists of two FDIs and two coils as shown in Fig. 3.4[1]. The measurement coils are modeled as a voltage source U_n together with an impedance R_{C}. Due to the compensation and the non-ideal resistances we have a systematic cross-talk between both measurement channels.

As this is a linear circuit we can describe it with the following linear set of

[1]Not pictured in this circuit diagram is the multiplexer and the other coils. The correction factor that we going to derive here, doesn't depend on the state of the multiplexer, as long as the resistance of each coil is similar enough.

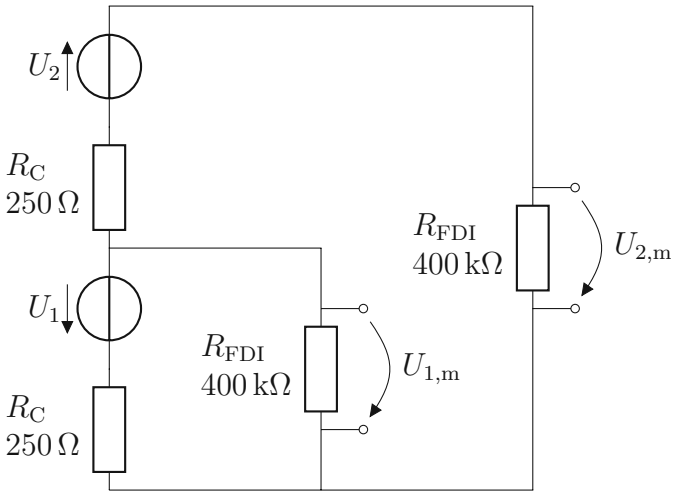

Figure 3.4: The measurement circuit consists of two coils and two FDIs. We model the coils as a voltage source U_n and an impedance R_C and the FDIs as a high resistor R_{FDI} with an ideal voltmeter $U_{n,m}$. The multiplexer is not shown here.

equations

$$\begin{bmatrix} U_{1,m} \\ U_{2,m} \end{bmatrix} = \underbrace{\begin{bmatrix} f_1 & k_{12} \\ k_{21} & f_2 \end{bmatrix}}_{=K} \begin{bmatrix} U_1 \\ U_2 \end{bmatrix}. \tag{3.6}$$

If the FDI input resistance would be infinite, the transformation matrix K would be

$$K_i = \begin{bmatrix} 1 & 0 \\ 1 & -1 \end{bmatrix}. \tag{3.7}$$

We can analytically solve this circuit for finite input resistance. Using the design values given by our components gives us a deviation from the ideal matrix

$$K_i - K = \begin{bmatrix} 12.7 & -6.4 \\ 19.1 & -12.7 \end{bmatrix} \times 10^{-4}. \tag{3.8}$$

We verified those values experimentally, by replacing the coils with a well-known voltage source and a resistor in series. For the correction we used the calculated factors using the individual measured resistance for each coil.

See Fig. 3.5 for an illustration of the effect of the correction. The upper plot shows the measured integral homogeneity profile and the lower plot shows the

results from the central coil. We recall that the central coil is always measured together with a compensated coil. Results from the central coil are plotted corresponding to the compensated coil used for this cycle. The lower plot clearly shows the coupling between the compensation coil and the central coil if we would use K_i. By using the corrected K we can improve by around an order of magnitude. Not evident in the figure is the absolute difference, which of course is a cogent reason as well.

3.1.3 Position offset between runs

We expect the results of a run to be independent of the running direction. So the go-run and the return-run should give us the exact same value, assuming a symmetric sensitivity function (see Eqn. 2.12). As a result of the arbitrarily placed index markers, in general an offset between the go- and the return-run is created; a detailed explanation is given in the following paragraph.

The encoder controller divides the step-trigger pulses generated from the encoder, down to lower resolution with an adjustable factor. This is done to reduce the amount of data and release the requirements on the measurement hardware. Let us assume we use a division factor of four, so the controller forwards every fourth pulse. The controller starts counting as soon as it is enabled and receives the first index pulse. Then again stops the forwarding immediately after the second index pulse. Note that, the number of step-trigger points between the two index markers is in general not a multiple of the preset division factor. When the encoder returns, the latter index marker becomes the first and starts the counting. Now again, the first step-trigger pulse is forwarded with the first marker. At this point we have an offset between the triggers from the go- and the return-run, in Fig. 3.6 this issue is illustrated.

This gives a shift δz between the two runs, which is below the step size Δz. It is worth to point out that the signals are not just shifted to each other, as in a trigger point is missing. But the measurement segments are not on the same position, see Fig. 3.6.

To correct for this we do a linear interpolation between the trigger points. The interpolation points are derived from the original sampling points shifted by the offset δz. This way, go and return signals are sampled at the same position. The effect of the correction becomes apparent in the regions with a strong field

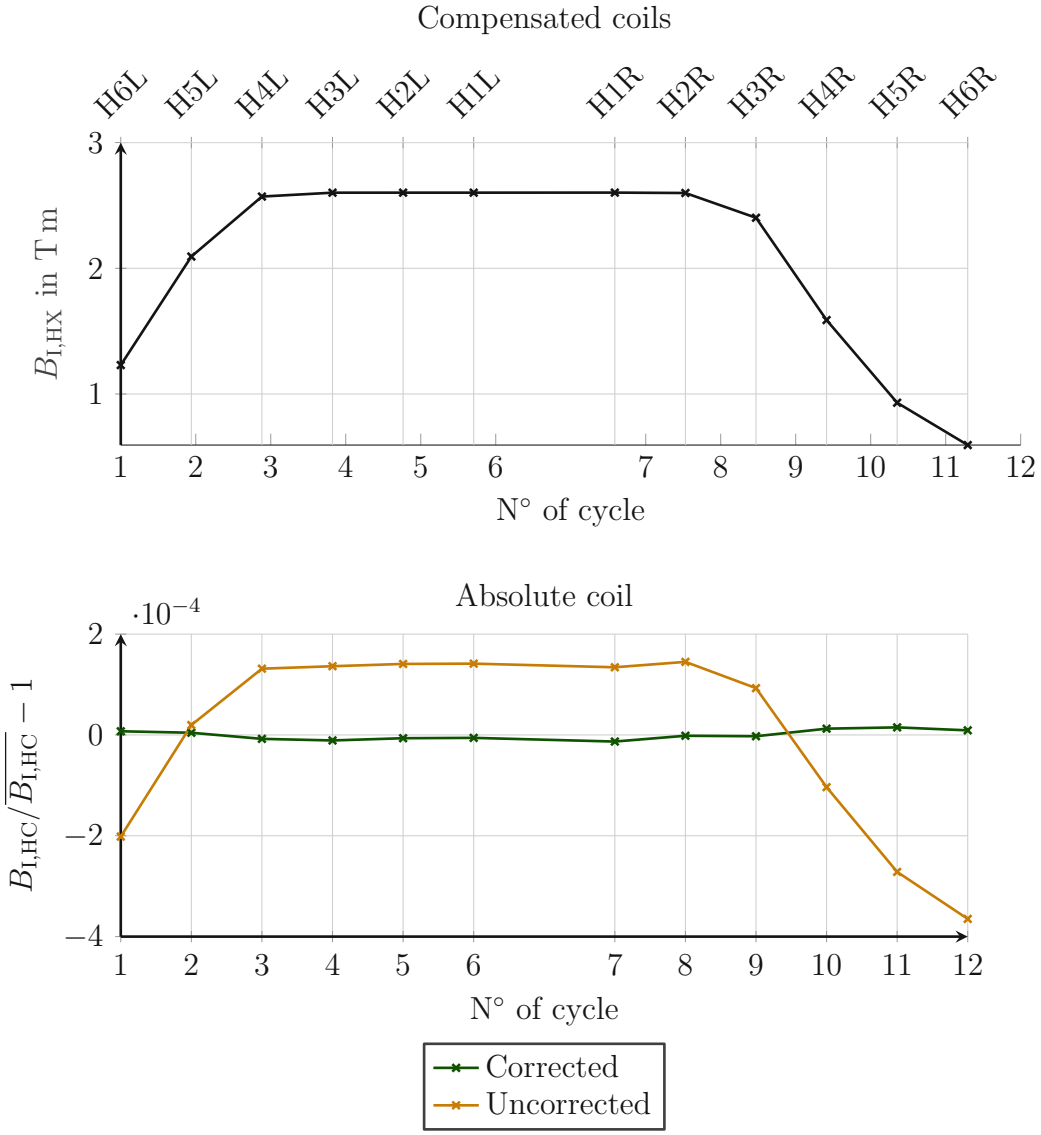

Figure 3.5: During a full measurement we measure a different compensated coil but the same absolute coil in each cycle. This correspondence is given with the top and bottom abscissa of the upper plot, which shows the integral on each compensated coil. The lower plot depicts the relative change of the integral of the absolute coil, measured at different cycles. Number of cycle of the absolute coil corresponds to the one from the compensated coils. For the uncorrected result —×— we used K_{i} and for the corrected result —×— we used K from Eqn. 3.8.

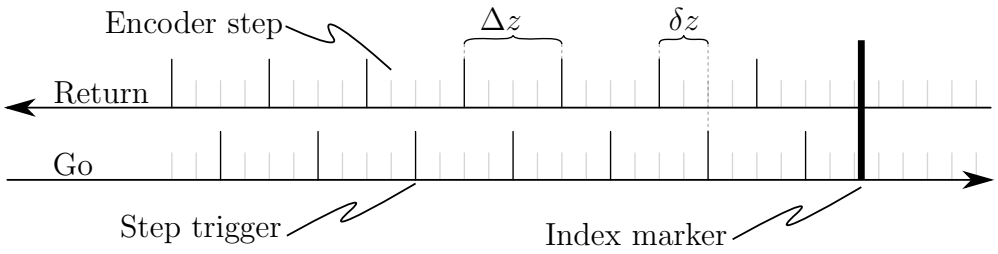

Figure 3.6: A systematic shift between the go- and the return-run trigger positions is connected to the division of the trigger signals and the position of the index markers.

change. The influence of the correction is depicted as difference between go and return run in Fig. 3.7. To acquire these signals we used the setup explained in Sec. 4.1.

This systematic offset depends on the division factor of the encoder controller and also on the position of the index markers. If one of these changes, we need to reestablish the offset. In order to ascertain the offset we oversample the signals by a linear interpolation between the points. A cross correlation between the go- and the return-signal shows the position where both signals have the maximal overlap. We do this for a bigger amount of measurements, typically around 100, so we can average out small deviations. This can be done for arbitrary division factors.

We recommend to do this for all factors, after first installing the system, in order to be independent on the choice of the division factor. The offsets used for the setup in Sec. 4.1 are listed in Table 3.1. We round the offset δz to multiples of 5 µm as this is the encoder strip resolution.

We want to point out, that neither the go nor the return run are wrong. They acquire the data at slightly different positions. The correction is necessary when the results from both runs are combined to reduce measurement noise.

3.1.4 Drift correction

The measurement devices, especially the integrators, need to provide a low uncertainty. A particular uncertainty is introduced by the integrators drift, as further described in [22]. The drift can arise from an offset voltage. This can originate anywhere in the circuit, for example at connectors or internally in

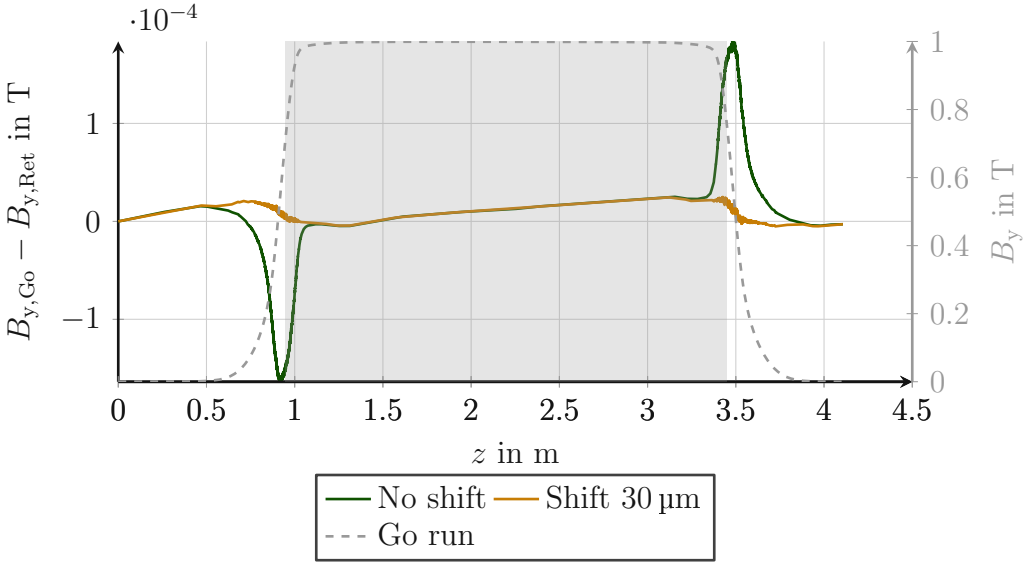

Figure 3.7: For —— no shift was applied. For —— a shift of $\delta z = 30\,\mu m$ was applied on the return signal in respect to the go signal. For reference the magnetic field of the go run is plotted on the right ordinate and the position of the magnet pole is indicated as gray shaded area.

Division factor	Stepsize Δz in µm	Offset δz in µm
4	80	30
8	160	30
16	320	190
32	640	510
64	1280	510

Table 3.1: Identified offsets for different encoder division factors from the setup used in Sec. 4.1.

the FDI and can have various reasons. This offset is integrated as well and depicts as a linear drift [22]. Also internal instabilities cause a drift - which is not necessarily linear [23][24].

However, the linear drift can be removed. When the slope of the drift is known, we can subtract it from the accumulated flux. To find the slope, we use the knowledge that, as long as the magnetic field is static, the start value must be equal to the end value of a cycle. The slope constant is chosen in order to fulfill this physical particularity. We describe the signal afflicted with a linear drift as

$$g(t) = f(t) + e(t) \quad \text{with} \quad e(t) = kt. \tag{3.9}$$

When we introduce the fact that at the start and end position we must have the same value $f(t_{\text{end}}) = f(t_0)$ we can determine the constant k_{drift} as

$$k_{\text{drift}} = \frac{g(t_{\text{end}}) - g(t_0)}{t_{\text{end}} - t_0}. \tag{3.10}$$

Now we know the error function $e(t)$ for the linear drift and we can correct it. Note that the drift happens on a time basis rather than on a spatial basis. As we acquire the data on a spatial basis, we need to know the timing of the signal, in order to be able to apply this correction. This maps $z = 0$ to $t = t_0$ and $z = z_{\text{end}}$ to $t = t_{\text{end}}$.

The drift constant can and needs to be calculated individually on every cycle, because the value slightly changes with time. A study of a long measurement including 120 cycles in a row, gave a mean value of $4.1 \times 10^{-13}\,\text{V s/s}$ with a standard deviation $\sigma = 5.2 \times 10^{-14}\,\text{V s/s}$. In relative numbers, the standard deviation is pretty big with more than 10 % of the mean value. This shows

that the drift is not constant and might also change within one cycle. It is also worth noting, that those 120 cycles are composed of 12 sets of cycles. Hence, the network changed slightly which explains a variation of the drift constant from cycle to cycle. When we do the same statistics, but only using the separate set of cycles, we see that the standard deviation is reduced by a factor of 2.

A further tactic to estimate the drift constant is to include a certain waiting time. During this period neither the carriage shall move nor shall the magnetic field change. The drift constant corresponds directly to the measured delta flux divided by the time duration. We don't expect an improvement to the method above, as the underlying principle is the same. We rather expect a decrease in the precision, because the determination of the constant happens at another point in time - it might already have changed when we do the run. Also it increases the total measurement time.

3.1.5 Flux offset

The translating fluxmeter is only capable of measuring a change of flux. To know the absolute field we would need to start at a point where the field is for sure zero. Theoretically this is never true but in practice we can neglect the field by starting far outside of the magnet.

Another way is to measure the field by other means at the starting point. In our case this is achieved by using a hall probe which is fixed to the PCB. We measure the local field and multiply it with the effective surface of the coils. This is then used as a starting value Φ_0 in Eqn. 2.7.

To be an effective method, it requires the starting point still to be in a region with a small field variation. This is needed because we measure the field locally at one point and extrapolate it to the rest of the coils' areas. In order to decrease the noise from the hall probe signal, it showed that it is advantageous to acquire data over a few seconds at the starting position.

4 Metrological Characterization

A novel measurement device requires an elaborated study on the quality of the measurement results. These studies shall give us information on the reliability and stability of the results, and eventually discover further influences. To obtain the complete metrological characteristic of the translating fluxmeter our studies intend to span a wide spectrum.

4.1 Measurement setup

At the magnetic measurement section at CERN a magnet commonly used for reference purposes is a former bending dipole magnet. This reference magnet is a C-shaped magnet with a 2.5 m long pole, a pole gap of 80 mm and a pole width of 350 mm. It is typically used with a nominal current of 316 A which induces a nominal field of 1 T. Although the dipole magnets for the Super-FRS are specified with a larger aperture, a stronger nominal field and are H-shaped, the reference dipole is a suitable magnet for our measurement campaign. The lengths of both types are in the same range and both have a quadrupole component due to their design. Thanks to the C-shape we can fit the 500 mm wide PCB into the magnet, although only a few coils are in the homogeneous region.

The length of the translating fluxmeter is about double the pole length. For this reason we designed and built a support structure, which is mounted to both ends of the pole. All components that are close to the field region are non-magnetic. See Fig. 4.1 for the translating fluxmeter installed in the reference dipole together with the support structure.

Pole width and width of the main plate are about the same, so when the translating fluxmeter is centered on the pole, the entire width is laying flat on the pole. The PCB is not centered on the carriage in order to fit into the

Figure 4.1: For the metrological characterization campaign the translating fluxmeter is installed in the reference dipole. The orientation of the coordinate system used in this work is shown here. For the location of the origin refer to text and Fig. 4.2.

magnet. It is shifted to the outside, so in positive x direction. Therefore, the central coil typically does not measure along the center of the magnet.

The coordinate system used in this work is oriented like the one commonly used for accelerator magnets, with the origin of z being the first index marker, see Fig. 4.1 and 4.2. Note that some measurement series might have a slightly different position and are therefore not strictly comparable among themselves. However, for the final measurement campaign the alignment can be assured by reference points on the main plate. It is foreseen to equip the plate with targets for a laser tracker. Together with the fiducial points of the magnet, the results from the translating fluxmeter can be referred to the magnet's frame.

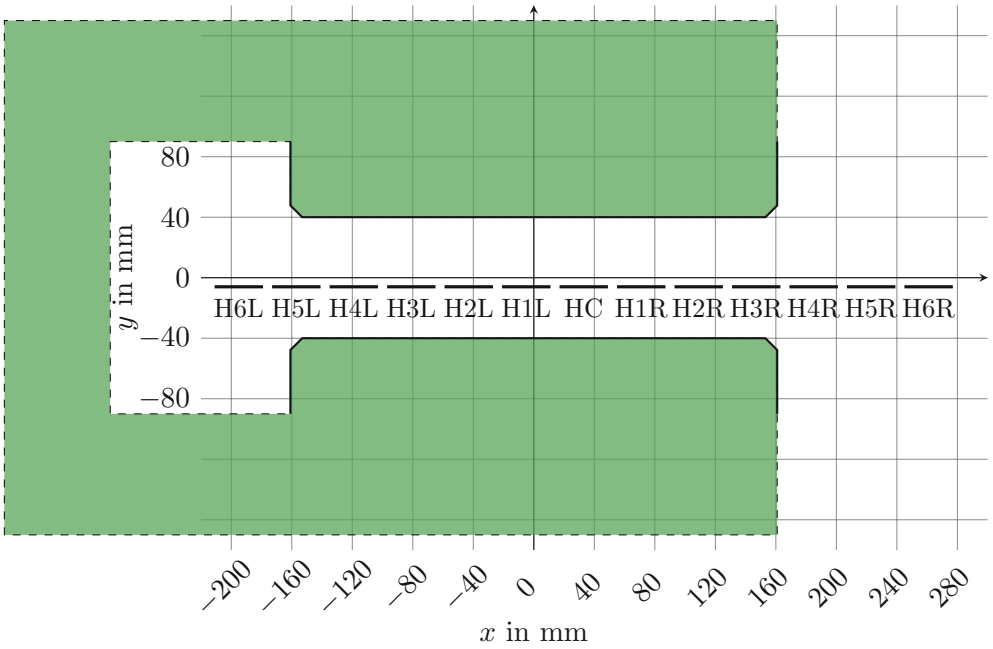

Figure 4.2: Origin of the xy-frame is centered in the magnet's aperture. The positions of the measurement coils HX as used in the majority of the measurements are depicted as black lines. The magnet's yoke is illustrated in green. Note that excitation coils are not shown and the dashed part of the yoke is not to scale.

4.2 Large sample statistics

An important quality factor for a measurement device is the repeatability. When we neither change the parameters of the device nor change the field to be measured, we expect to get the same result for different measurements. The spread of the results from such a measurement series, typically defines the noise level of the device. If this spread depicts a suspicious trend, it could point to a not yet fully understood effect that needs further research.

We run a measurement series with a fixed set of parameters, with the translating fluxmeter placed centered on the pole. The fluxmeter was driven with a goal velocity of 0.56 m/s, the encoder generated a step-trigger every $\Delta z = 160\,\mu\text{m}$. The ac-/deceleration was set in a way that the goal velocity was reached after 97 mm - the first index marker typically was crossed a few mm after the goal velocity was reached. So we avoid to have a change in the velocity during the measurement. We powered the magnet with a nominal current of 316 A, which leads to a nominal field of 1 T.

The measurement series consisted of 12 set of cycles with 10 cycles for each compensated coil. This leads to in total 120 cycles and 240 acquired runs with the absolute coil, which gives us a solid set of data to perform statistical analyses. The entire measurement was running non-stop and took in total 64 min.

The averaged results from this measurement campaign is shown and discussed first, followed by a statistical analysis of various aspects. For the evaluation of the results we used an absolute surface $A_{\text{HC}} = 0.4847\,\text{m}^2$ for the central coil and an inhomogenity profile as obtained from the in situ calibration shown in Fig. 3.3. We resign from showing the results from the far outer coils HL6, HR5 and HR6. For solving Eqn. 2.12 we follow the naive approach from Eqn. 2.8.

Average We used the entire set of data from this measurement to calculate an average. First we study the longitudinal results. With 10 coils we can sample a large area with a high range, see Fig. 4.3. A close up on the homogeneous field region reveals smaller variations, see Fig. 4.4.

Another perspective is given by the transversal view. With the set of $B_{\text{I,HX}}$ we can obtain a profile in x. Typically the profile in x is used as transversal

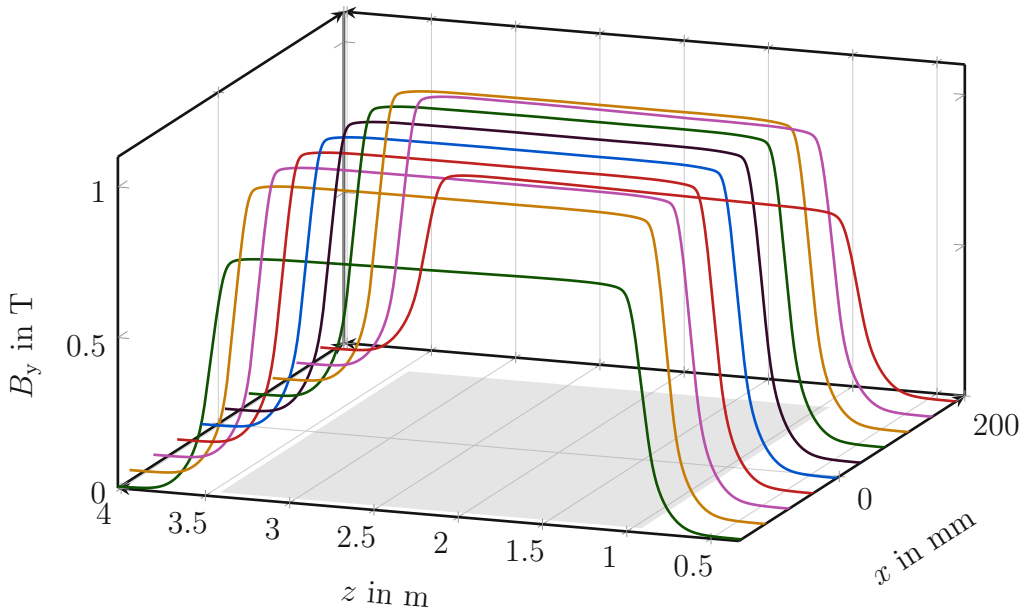

Figure 4.3: Longitudinal profile of 10 coils in relation to the position of the pole (depicted as grey shaded area).

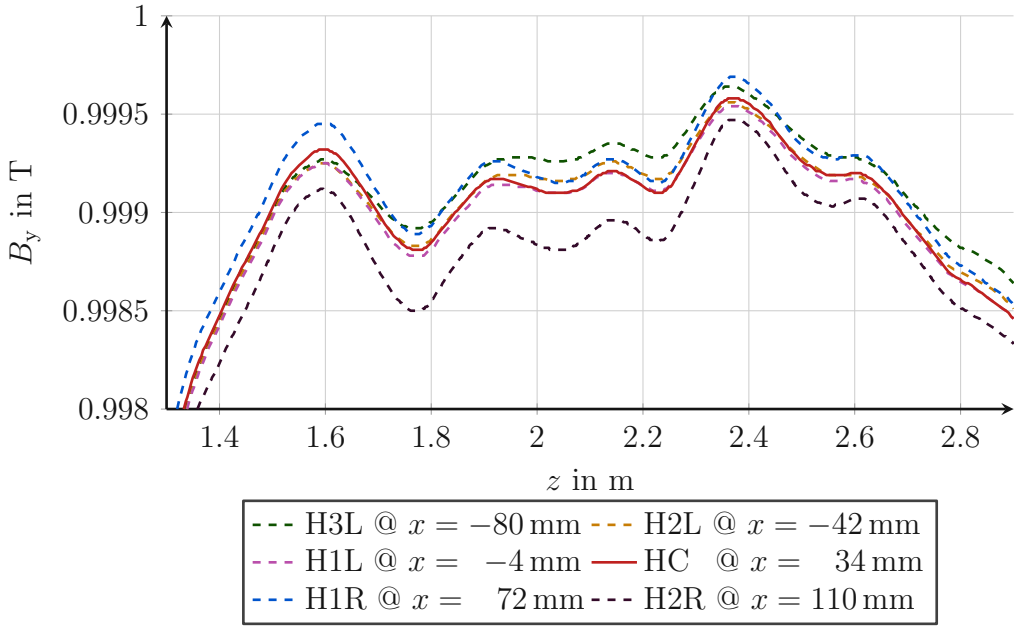

Figure 4.4: Longitudinal profile of the homogeneous field region covered by 6 coils.

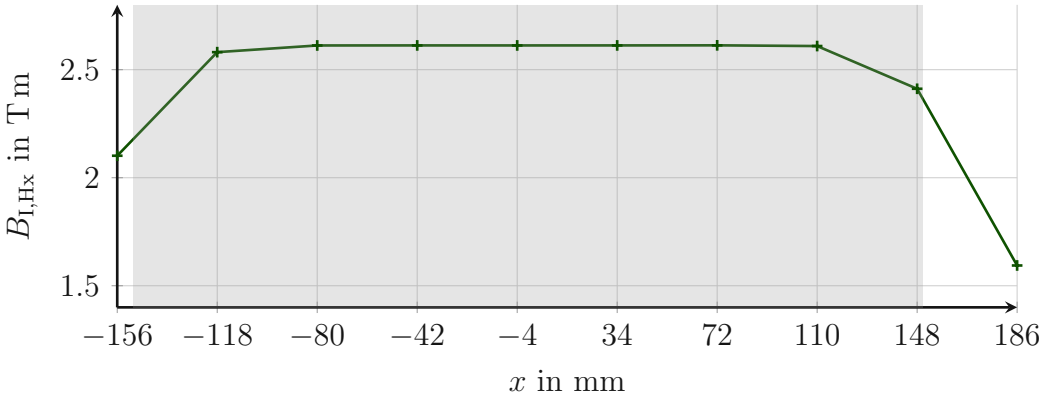

(a) Absolute transversal field profile, with the position of the pole shown in grey.

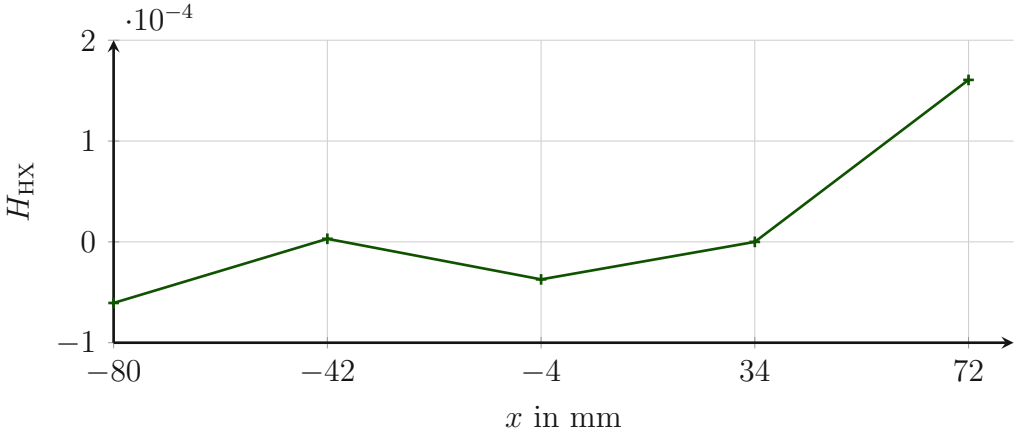

(b) The integral homogeneity for the inner region.

Figure 4.5: The transversal field profile shows the integral fields of each coil.

homogeneity

$$H_{\mathrm{HX}} = \frac{B_{\mathrm{I,HX}} - B_{\mathrm{I,HC}}}{B_{\mathrm{I,HC}}} \tag{4.1}$$

for qualifying the field quality of magnets.

The field profile given by the absolute integral values $B_{\mathrm{I,HX}}$ is shown in 4.5a. While the transversal homogeneity is only shown for the 5 most inner coils in Fig. 4.5b.

Variation We used the 240 runs on the absolute coil to estimate some limits for the variation. To get a better understanding on the contribution of each part we divide the measurement path $\mathscr{S}$ into three zones. The outer zones $\mathscr{S}_I$ and $\mathscr{S}_{III}$ cover mainly the field at the end regions, while the inner zone $\mathscr{S}_{II}$ covers the homogeneous field region, as marked in Fig. 4.6. Together all three zones cover the total measurement path $\mathscr{S}_\mathrm{T}$.

This yields the results from Table 4.1 with the definitions

$$\overline{B_\mathrm{I}(\mathscr{S})} = \frac{1}{J}\sum_{j=1}^{J} B_{\mathrm{I},j}(\mathscr{S}) \tag{4.2}$$

$$\sigma_{abs} = \frac{1}{J}\sum_{j=1}^{J}\left(B_{\mathrm{I},j}(\mathscr{S}) - \overline{B_\mathrm{I}(\mathscr{S})}\right)^2 \tag{4.3}$$

$$\sigma_{rel} = \sigma_{abs}/\overline{B_\mathrm{I}(\mathscr{S})} \quad , \tag{4.4}$$

where the index j stands for the number of the cycle and J for the total amount of cycles. We saved on the notation by omitting the coil's label because all calculations can be applied to each coil independently.

$\mathscr{S}$	$\overline{B_\mathrm{I}(\mathscr{S})}$ in T	σ_{abs} in 1×10^{-5} T	σ_{rel} in 1×10^{-4}
Zone I	0.514	1.064	0.207
Zone II	1.589	1.857	0.117
Zone III	0.510	2.046	0.401
Total	2.6123	2.291	0.087

Table 4.1: Integral field and corresponding standard deviation itemized in three zones calculated for the central coil HC.

The results in Table 4.1 for the coil HC devolve also to the remaining coils. We observed no significant difference between the σ_{rel} of different coils. Noticeable is an higher σ_{rel} in zone III than in zone I. It seems that this increase coheres with the integration. When we start the summation of the delta fluxes from the other side the effects turns around. Also we cannot find this effect with delta fluxes.

A visual representation of the standard deviation along the entire measurement range is shown in Fig. 4.6, where the standard deviation is calculated for each

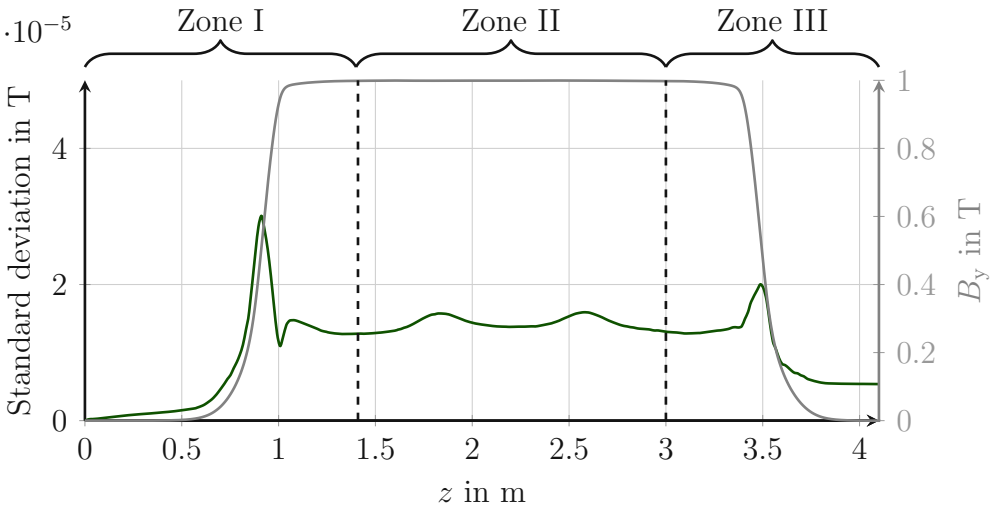

Figure 4.6: The standard deviation calculated for each point in z shown in comparison to the evaluated flux density of the central coil HC. Additionally, the location of the zones are shown.

point in z. The peaks in the standard deviation are located where the magnetic field rises/falls. This can be explained by a high sensitivity to a displacement, mainly in z but also in x and y.

To further investigate the distribution of the results, we had a look at the spreading of the results at three specific points, see Fig. 4.7. The histograms are shifted by their individual mean values, in order to give a better scale of the amplitudes. At the two points in the fringe field we can identify two accumulations. They probably yield from a slight offset between the go and return run. In a first approximation the distribution for the middle point and the individual accumulations can be described by a normal distribution. For a better description we require a study with a larger sample size.

Again, we also have a look at the transversal view. Here, the standard deviation is given by the integral of the individual coils. Using the field integral $B_{\mathrm{I,HX}}$ shown in Fig. 4.5a as reference, we calculate the relative standard deviation $\sigma_{\mathrm{abs,HX}}/\overline{B_{\mathrm{I,HX}}}$ on each coil, see Fig. 4.8. Note that the amount of statistical data on the absolute coil is by a factor 12 bigger than on the others. This relative standard deviation is well below 1×10^{-5}, so we have an excellent repeatability on the integral.

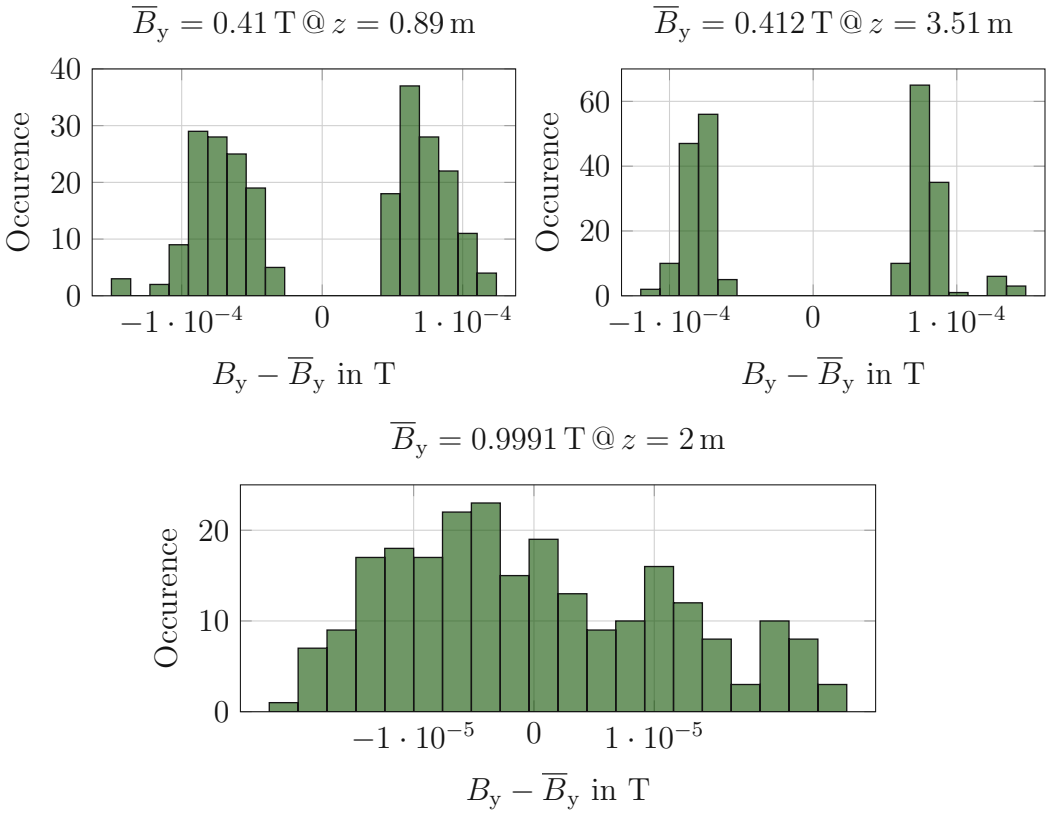

Figure 4.7: Histograms calculated using the 240 runs of the central coil. Each histogram is calculated at a different position in z and shifted by the local mean value $\overline{B}_y$.

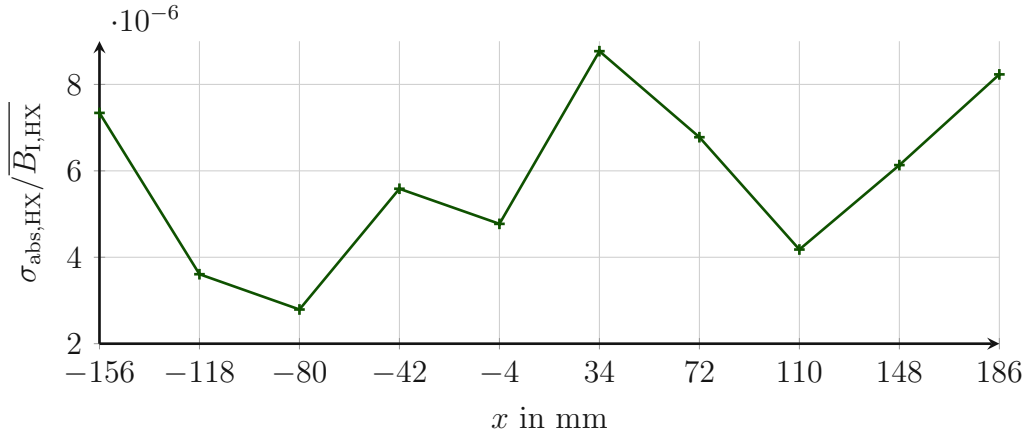

Figure 4.8: The relative standard deviation of the integral is well below 1×10^{-5} for all coils. The central coil HC is located at $x = 34\,\mathrm{mm}$.

4.3 Parameter study

Our system has a couple of parameters available to the user. In a study we want to find the sensitivity of the results to those parameters. This could reveal an optimum for the parameters or a possible unknown effect.

4.3.1 Velocity

The velocity is supposed to have no influence on the results, as we make use of the reparametrization (see Eqn. 2.6). The experiment for verification is relatively simple. The setup is the same as in Sec. 4.2, but with various slower velocities.

In the evaluation of the zone integrals we observed a slight dependence on the velocity, see Fig. 4.9. For this evaluation we calculated the relative change of the integral $B_{\mathrm{I},v}/\overline{B}_{\mathrm{I}} - 1$ to the average integral field $\overline{B}_{\mathrm{I}}$. We split the integral into the three zones to see if the end regions with strong field variation have any particular influence. The observed effect occurs in a small range of around 0.1 Units[1]. Further we didn't find any noteworthy change in the standard deviation caused by the variation of the velocity.

[1] Units is a term used to describe relative deviations, similar to ppm. 1 Unit corresponds to 1×10^{-4}

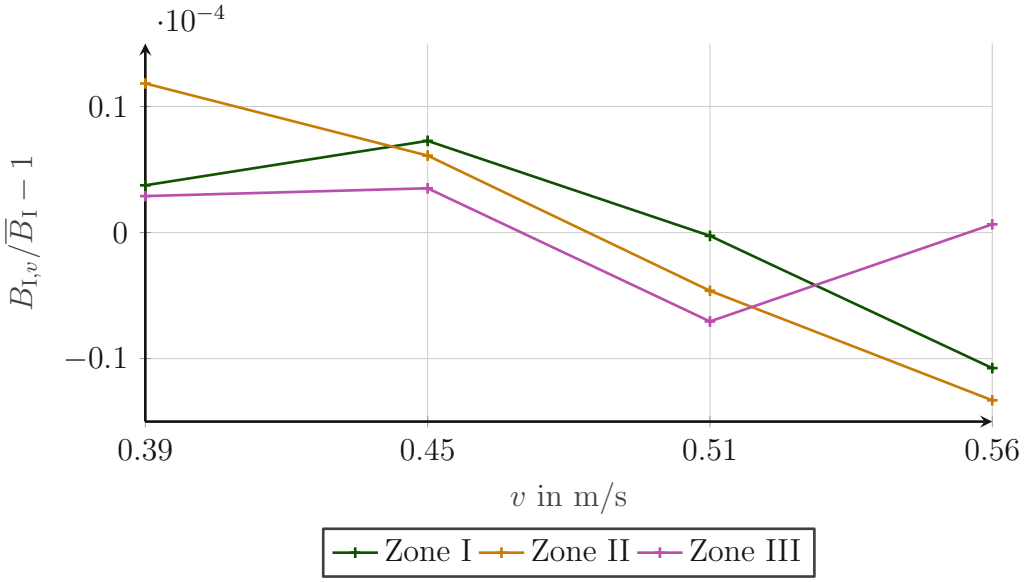

Figure 4.9: The relative change of the integral in dependence of the velocity v for each zone. While the shown values are only for the central coil, the other coils give similar results.

From our results it emerges that the trend would fit to an eddy current induced by the moving carriage. The eddy current only can be induced in the encoders housing, the connectors themselves or in the shorted loops. But we cannot exclude other explanations than eddy currents at this point. This observation would suggest to use rather slower velocities since the eddy currents typically increase with velocity.

Another essential study looks at the local velocity $v(z) = \Delta z/\Delta t$. We derived the local velocity from the step-triggers and their timing, which is recorded by the FDIs. This gives us the velocity projected on the trajectory of the encoder strip. Note that e.g. a snaking of the carriage might appear as a velocity change but actually is only more lateral distance traveled between two markers on the strip, see Fig. 4.10. So a change in $v(z)$ can be caused by either a varying local velocity or an altered path.

Results of $v(z)$ for various nominal velocities are similar, see Fig. 4.11. The relative standard variation for this velocity is above 1 %. We observed a decay of the oscillations at the beginning. This is improved by tensioning the drive

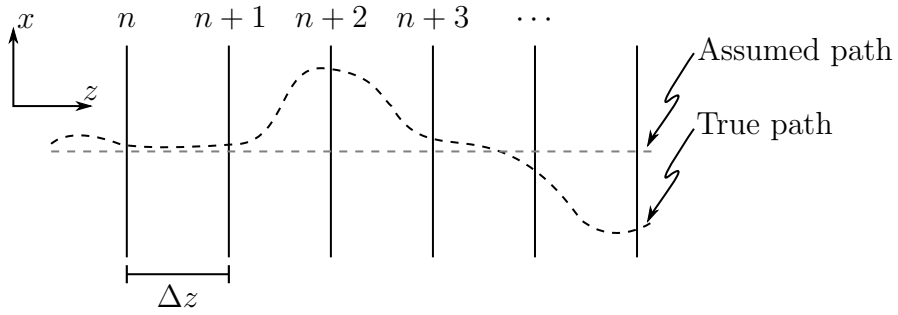

Figure 4.10: For the velocity calculation we assume a straight path, so the moved distance between n and $n+1$ is equal to Δz. The true path is unknown and could have some lateral motion. So the distance between n and $n+1$ would actually be longer.

wire for the sliding carriage. The close up shows a clear sinusoidal component, this becomes even clearer looking at the power spectrum, see Fig. 4.12. It shows the spectrum of the velocity together with the spectrum of the measured flux. We can clearly see a correlation between those two spectra.

Let me point out the peak at $50\,\mathrm{m}^{-1}$. We found that this peak corresponds to the 2 cm long links of the cable chain. They produce vibrations while rolling off at the end of the translating fluxmeter, which are transmitted to the carriage. We verified this with a small measurement, where we supported the cable chain by hand. That way we excluded this source of vibrations. In the spectrum we could observe the peaks at $50\,\mathrm{m}^{-1}$, $100\,\mathrm{m}^{-1}$ and $150\,\mathrm{m}^{-1}$ to disappear.

Another source of vibrations connects to the sliding mechanism. When the driving force is not split perfectly 50:50 on each rail, one side advances until it gets slightly stuck and the other side catches up. This causes a kind of wobbling movement.

In terms of variation, the velocity doesn't seem to effect the results. The relative standard deviation of the integral field calculated for different velocities is constant down to a range of 0.05 Units. Data (see Fig. 4.11) and practice showed that slower velocities have higher relative vibrations. We therefore recommend to use a velocity between 0.5 m/s and 0.6 m/s.

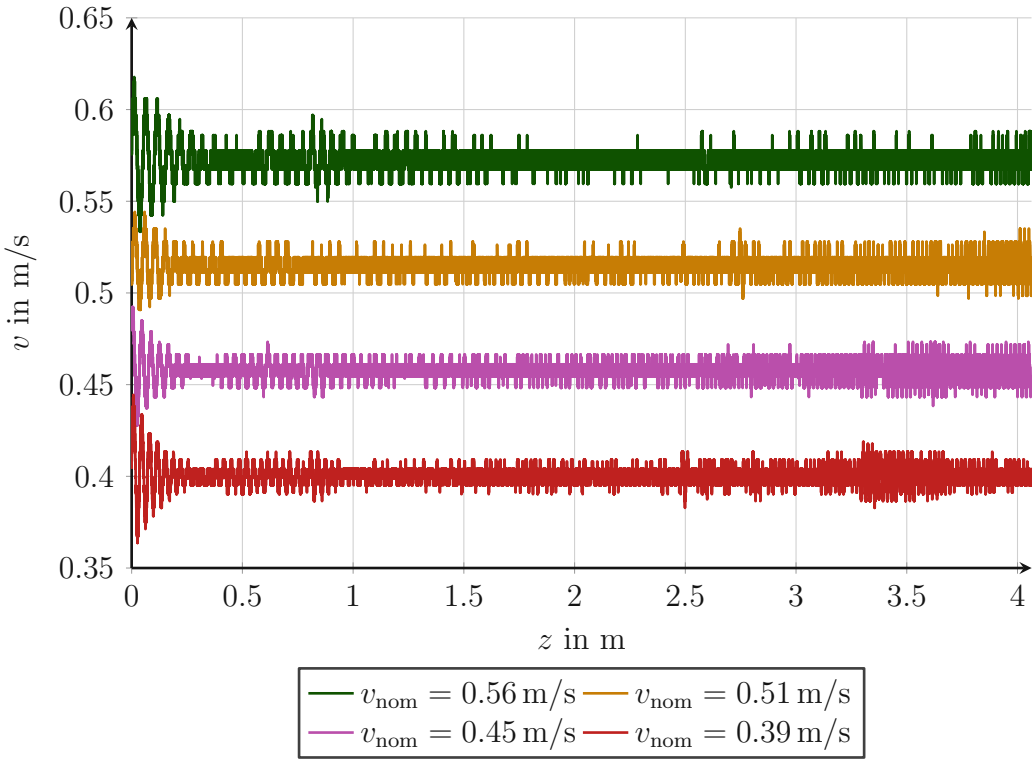

Figure 4.11: The velocity $v(z)$ for 4 runs, each with a different nominal velocity v_{nom} are derived from the timing of the triggers recorded by the FDI.

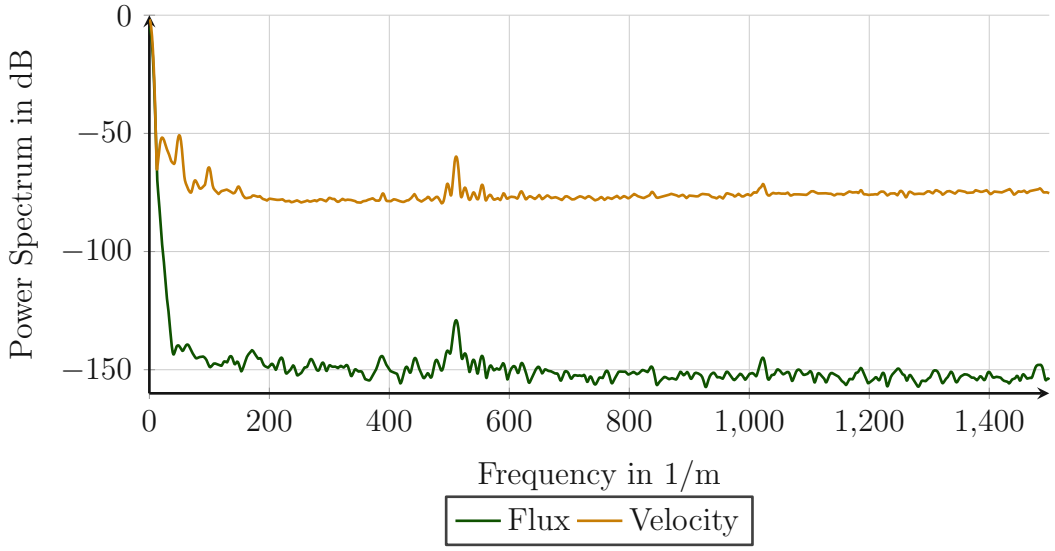

Figure 4.12: The power spectrum of the measured flux and the corresponding local velocity $v(z)$, whereas $v_{\text{nom}} = 0.56\,\text{m/s}$.

4.3.2 Encoder divisor

Obviously the encoder divisor has a major effect on the longitudinal resolution. This resolution should not effect the result of the integral field, which is assured by the use of an integrator. A measurement series where we only varied the division factor, proofed that this is valid. The relative standard deviation σ_{rel} across this measurement series gives 0.07 Units. For this evaluation we only looked at the integral field of the entire measurement range. We didn't follow the zone-wise strategy here because the partition of the zones leads to a sampling error. Further we can state that the noise level was equal for each divisor.

As discussed in Sec. 3.1.3 we need to apply a shift. For executing this shift, we do a linear interpolation. When the stepsize Δz becomes longer, the linear interpolation becomes less accurate. Therewith the introduced error is increased. The alignment between the go and return run with $\Delta z = 1.28\,\text{mm}$ and $0.64\,\text{mm}$ already showed major differences. This asks for small division factors. Using 4 as a division factor results in a high data rate, which reaches towards the limits of the FDIs. We therefore recommend to use 8, which is small enough and still doesn't push the FDI to its limits.

4.4 Multiplexer

Most of the components used in the setup of the translating fluxmeter are well known and tested parts. The multiplexer, that we use to reduce the needed amount of FDIs, was developed at CERN specifically for this setup. So we want to dedicate it a special focus in this section - especially as it directly handles the measurement signals. The multiplexer has to handle two main tasks. First to connect the chosen coil to the output and second to do the compensation.

The first task is working just fine, without adding any significant resistance to the circuit. To verify the second task, we compared a standard measurement similar to the one from Sec. 4.2 with a measurement where we manually patched the coils on a patchpanel.

We found a small offset between the integral fields for the two measurements. The offset changes slightly from coil to coil but this variation is within the limits of the variation from Table 4.1. The average offset for the total integral field is $-6 \times 10^{-5}\,\mathrm{T\,m}$ from the measurement with multiplexer to the one without. In relation to the integral field of the absolute coil this corresponds to -0.024 Units. We assume that this difference comes from a change of resistance of the circuits. Further we didn't find any deviations between those two measurements.

4.5 Mechanical evaluation

It is obvious that the mechanics of the system can strongly influence the results, by changing the trajectory of the sliding carriage. Ideally we want the trajectory to be as straight as possible, independent from mechanical intervention and repeatable from run to run. The condition for straightness covers two types. The first is a static one, bending. The second dimension expresses as a vibration, and tends to be unreproducible from run to run, but nevertheless has a certain regularity. All those factors are defined by the mechanical design but as well from the installation and alignment process. For this reason, we briefly describe the foreseen installation procedure and present anticipated mechanisms to assure a stable trajectory.

The main plate is not designed to be rigid enough to prevent bending. It relies on the support it is placed on. Within a magnet this is ensured, because it lies on the pole, which typically is flat enough for this purpose. The translating

fluxmeter is designed to reach out of the magnet, therefore it needs a support for the part outside of the magnet. This needs to be designed for each magnet under test. For the storage, a dedicated table is used which is engineered to give a proper support to the translating fluxmeter. This table is also included in the testbench design for the Super-FRS dipole. It will be placed in the prolongation of the magnet in a way that the translating fluxmeter can be directly slid longitudinally into the magnet. This way an even support is ensured during the entire measurement campaign.

When the translating fluxmeter needs to be lifted off the table, a dedicated lifting device needs to be installed. The main plate is prepared with two T-profiles on the two long sides. Their purpose is to give hold to massive and rigid aluminum profiles. Those profiles are equipped with hooks, that are placed at a very specific distance. Their location is chosen on the mass distribution of the entire device, in a way that a minimal force acts on the plate when it gets lifted at those points. After lifting the device, the aluminum profile together with the hooks needs to be removed before measurement.

For the evaluation of the mechanical characteristics, we used a Laser Tracker AT930 from Leica. For the measurements of the trajectory we used a non-magnetic 0.5 inches reflector that was fixed temporally to the carriage. For locating the translating fluxmeter itself, we used reference points on the plate which can hold a 1.5 inches reflector.

The internal coordinate system of the measurement software for the laser tracker was aligned with the coordinate system of the magnet. This allows us to easily read out the deviations to an ideal trajectory. We fitted a line to the point cloud and calculated the normal distance of each point to this ideal line. The normal distance is composed of a x and a y component. These deviations don't show any misalignment of the translating fluxmeter to the magnet, as this is filtered out by the line fit.

We measured the trajectory 7 times. With each measurement the plate was shifted from its origin, in order to averages out small effects coming from the concrete position. Further this simulates the installation process during the measurement campaign in the Super-FRS dipole and we can estimate the stability. In Fig. 4.13 we show the deviations in x and y in two different plots. In each plot is the mean value shown from the 7 measurements together with the variation boundaries. The variation boundaries correspond to the

standard deviation of the 7 measurements added/subtracted to the mean value. Over the entire measurement length this gives a standard deviation for each direction $\sigma_x = 59.7\,\mu m$ and $\sigma_y = 410\,\mu m$. The curve shape for the deviation in y shows clearly that the ends are hanging down. At least a major part of it can be explained by the side support structures. Although they are on the same level as the pole, they are not as wide as the pole. The main plate is equipped with small plastic ball units on the bottom, to allow an easy moving. Our side support structure is not wide enough to give support to those ball units. The designed offset between the edge of the aluminum plate and the ball units is 2 mm. We assume this to be a major reason for the deformation in the y direction. This can be solved by adjusting the side support structure accordingly. It points out that we owe a significant importance to the ground support.

The mechanical deviations, see Fig. 4.13, effect the results of the translating fluxmeter in two ways. The first, being quite trivial, is that the measurements are recorded on a different location than actually expected. The second consequence manifests in the effective surface of the coils. A variation in the deviation tilts the PCB. A tilt in the PCB reduces the effective surface of the coils for B_y and may increase for skew components. Evaluating the data from Fig. 4.13b, shows that the inclination $k = \tan(\alpha)$ varies with $\sigma_k = 1.2 \times 10^{-3}\,rad$. The influence on the surface translates with $\cos(\alpha)$. We calculate a standard deviation $\sigma_\alpha = 1.3 \times 10^{-6}$. So the slightly bend plate effects the surface only in a negligible range. In case one wants to reduce this source of error as well, for example when the bending becomes too big, we can think about using a coil surface which depends on the position.

4.5.1 PCB mounting

Apart from the transport and moving of the entire system, one of the most frequently used parts is the PCB. This sensing element is supposed to be interchangeable in order to adapt it to other magnet systems. Also for the in situ calibration it gets dis-/mounted. This raises the challenge of ensuring the same position. The design took this issue into account and has foreseen two pins to precisely combine the PCB with the sliding carriage. Also the shims are aligned by pins. The bottom reference has two single holes for the pins, while the PCB has one hole and one elongated hole.

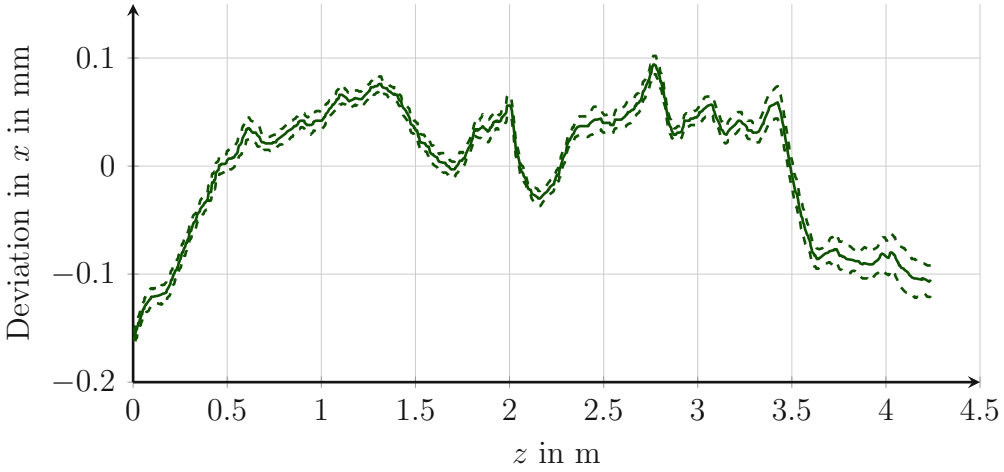

(a) Deviations in the x-direction

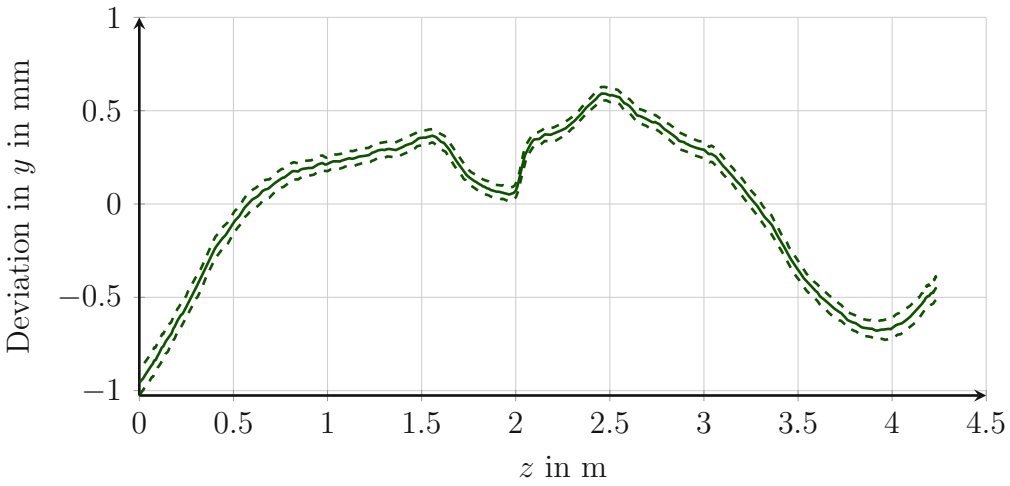

(b) Deviations in the y-direction

Figure 4.13: We calculated the deviation of the trajectory to a fitted line. The continuous line indicates the mean value and the dashed line indicates the variation based on the standard variation.

For verifying the repeatability we dismounted and directly remounted the PCB again. We tried to make sure to get the biggest possible variation, for example by removing the pins. After each remount we started a measurement and checked the results for any deviation. On none of the coils we could observe any changes from measurement to measurement above the standard deviation from Table 4.1. We found a hint that it is important to make sure all the four screws are properly tighten. For the production of the PCB it was difficult to obtain a flat board due to internal stress. Even the final version was not perfectly flat. The parabolic shape of the board caused an y-offset between the board's center in x to its outside of roughly 1 mm to 2 mm. The screws are deforming the board and pressing it towards the flat surface of the carriage. Consequently the fastening torque has an effect on this.

4.6 Comparison to standard measurements

While previous results characterized the translating fluxmeter in terms of stability and repeatability, we also want to compare the results to well established methods. There is no single method available that could be used for comparison, as the measured quantities of the translating fluxmeter are quite unique. For our purpose we found that the combination of two methods give us a valid base for comparison. For the longitudinal profile we used a NMR to obtain a profile in the homogeneous region. For the integral we can use results from a SSW measurement.

4.6.1 NMR

The Nuclear Magnetic Resonance (NMR) is a measurement device, with a high accuracy for magnetic measurements in homogeneous fields. Typically an accuracy of 0.1 ppm is achievable. The principle is found in the behavior of particles in a magnetic field. They exhibit a precession around the direction of the field with a certain frequency - called Larmor frequency. This frequency is directly proportional to the applied field with a particle inherent constant. There are a couple of different methods to measure this frequency. They are based on finding a resonance, doing so comes typically with an increased measurement time. The measurement uncertainty typically is linked to the measurement

time, thus fast measurements have a larger uncertainty [1].

This is a big disadvantage over the translating fluxmeter. To measure nearly as many points as done with the translating fluxmeter, it would take several hours up to days. Unlike the translating fluxmeter, the uncertainty of the field integral decreases with a bigger spatial resolution. Further more, the NMR needs a strict homogeneous field [1]. So we aren't able to measure the field along the entire length.

The setup of the translating fluxmeter was similar to the one in Sec. 4.2. We took a measurement with only a reduced set of coils, because we are mostly interested in the absolute coil. This measurement is used as a reference for comparing with the NMR results.

The NMR sensor head was mounted to the PCB, so that the center of the probe was above the center of the absolute coil. It is worth mentioning, there was an offset in y direction of about 7 mm with respect to the PCB. The carriage equipped with the NMR probe was moved manually through the magnet and each 16 mm we took a sample. We used the encoder and a trigger counter to determine the position of the carriage. Since the NMR requires a nearly perfect homogeneous field, we could not cover the same region as we can with the translating fluxmeter.

For the evaluation we applied a numerical convolution to the results from the NMR. For this convolution we used a hat-function for the sensitivity function with the same length as the coil and with an area equal to $1\,\mathrm{m}^2$. Since the NMR measures the field point-wise, we need to simulate the convolution. The result from the numerical convolution should correspond to the measured field from the translating fluxmeter. This numerical convolution is needed because so far we don't have introduced a proper deconvolution method for the translating fluxmeter.

After the convolution the results are smoother and correlate very precisely to the results from the translating fluxmeter, see Fig. 4.14. We find an offset between the two signals. We relate this offset with a wrong starting flux Φ_0. Unfortunately, for those measurements we don't have a reliable result of the hall sensor. It was broken due to its sensitive cabling.

We want to point out that the NMR also gives us a possibility to cross-check the calibrated coil surface. To do so, we perform a measurement as described

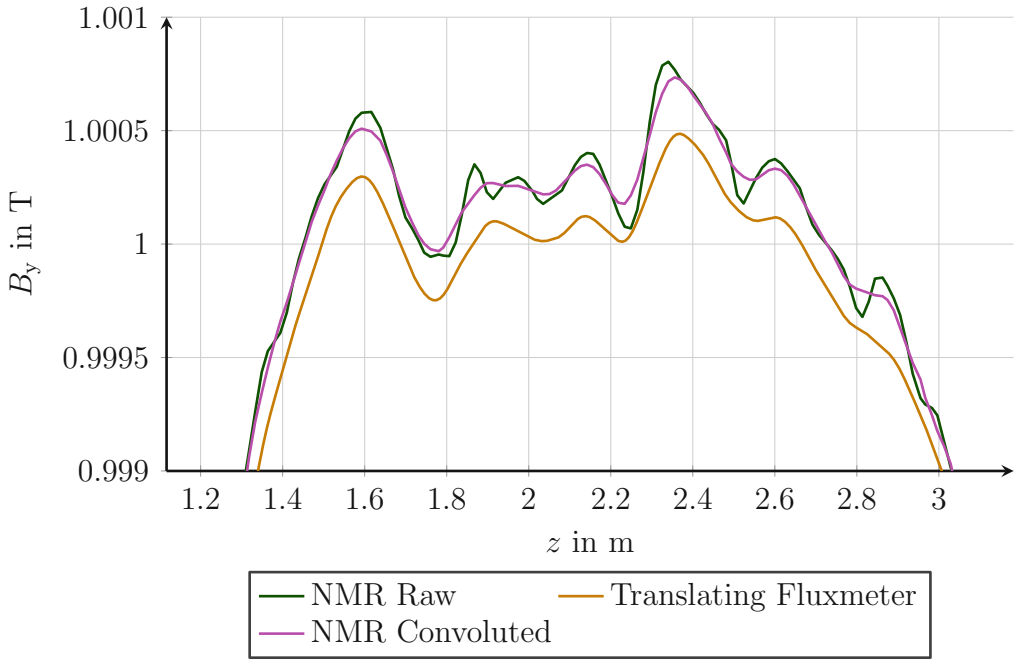

Figure 4.14: The raw data from the NMR is shown besides the post-processed convoluted one and the signal from the translating fluxmeter.

in this section. Then we need to find a factor to minimize the mean square error between the two curves. This factor can be used to find the coil surface. As explained in Sec. 3.1.1 we can obtain an accurate value for the surface from the designed track positions. The coil calibration in the reference dipole assists in form of a verification and with detection of faults. So we can use this degree of freedom to determine the offset Φ_0.

4.6.2 Single stretched wire

We use measurements from the single stretched wire to verify the integral homogeneity of the translating fluxmeter. The results of the SSW measurement were extracted from the published work in [25]. As reference we use the results from Sec. 4.2. We calculated the integral homogeneity using the central coil as reference coil as in Eqn. 4.1.

The H_{HX} for both, the SSW and the translating fluxmeter are shown in Fig. 4.15.

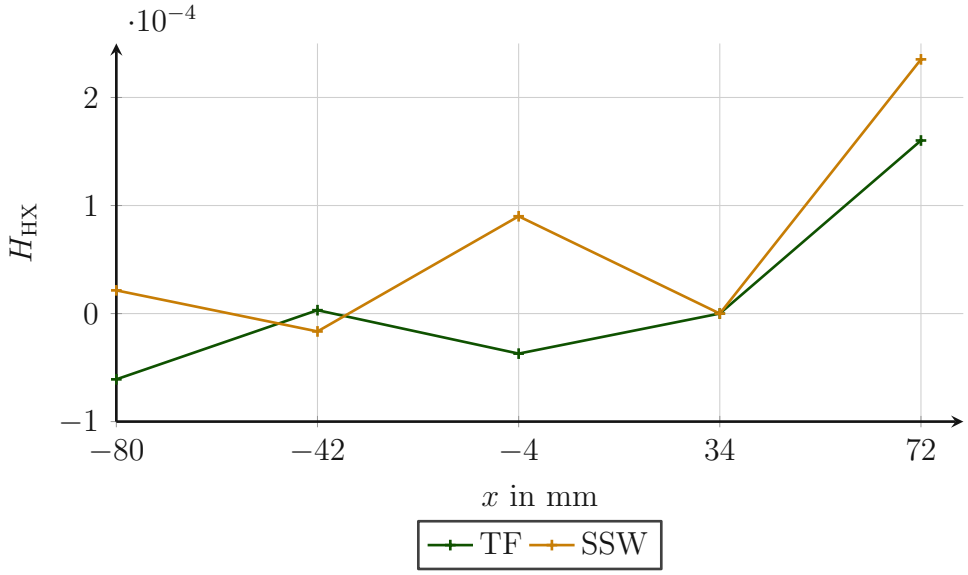

Figure 4.15: The integral homogeneity H_{HX} of the translating fluxmeter in comparison to the results from a SSW measurement at the according positions. SSW measurement data was extracted from [25].

The linear trend visible in both curves represents the quadrupole component of the magnet. These results do not fully satisfy the demands for the translating fluxmeter. We expect the results to improve when we execute the measurement with the SSW respecting the position and length of the translating fluxmeter. Also slightly different excitation states of the magnet can play a role.

5 Advanced Processing

From the derivation in Sec. 2.1 we know, that we need to solve Eqn. 2.13 to obtain $\overline{B}_y$ - to save on notation we will use B further in this chapter. This process is commonly known under deconvolution. There are a couple of established methods to tackle this problem. We need to evaluate those methods in order to estimate their utility for our case. We will discuss this problem in the spatial as well as in the frequency domain and highlight their core issues. After, we check an approach on a spline basis.

We will further present the multipole expansion in 3D together with some results based on measurement of the translating fluxmeter.

5.1 Deconvolution

5.1.1 Spatial domain

First we consider our measurement as a problem on a spatial discrete domain. As indicated in Eqn. 2.7 we can assign each grid point n a flux Φ_n. We transform the convolution from Eqn. 2.13 to a discrete convolution

$$\Phi_n = \sum_{k=0}^{K} B_k PSF_{n-k} \tag{5.1}$$

where PSF_n is the kernel of the convolution with $PSF_n = \widehat{F}s(\Delta zn)$. Such a discrete convolution can be written in a vectorial way [26]. We write our input signal $B_n, n = 0, 1, \cdots, L-1$ as a vector $\mathbf{B} \in \mathbb{R}^L$ and assume the field for $n < 0$ to be zero. The PSF_n is a finite sequence describing the non-zero part of the point spread function with $n = 0, 1, \cdots, M-1$, forming the convolution

matrix

$$\mathbf{S} = \begin{pmatrix} PSF_0 & \cdots & \cdots & 0 \\ PSF_1 & PSF_0 & \cdots & 0 \\ \vdots & \ddots & \ddots & \vdots \\ 0 & \cdots & PSF_{M-1} & PSF_{M-2} \\ 0 & \cdots & \cdots & PSF_{M-1} \end{pmatrix} \tag{5.2}$$

This way we can describe our convolution problem as

$$\mathbf{\Phi} = \mathbf{SB}, \tag{5.3}$$

where $\mathbf{\Phi} \in \mathbb{R}^{L+M-1}$. With respect to the system we can truncate the convolution at the end so $K = L - 1$. We truncate the M-last lines from the matrix $\mathbf{S}$ and obtain $\mathbf{S}'$, which is a square matrix.

With $\mathbf{\Phi} = \mathbf{S}'\mathbf{B}$ we have a linear set of equations. If we can find an inverse of $\mathbf{S}'$, we can solve the deconvolution by solving the inverse problem

$$\mathbf{B} = \mathbf{S}'^{-1}\mathbf{\Phi}. \tag{5.4}$$

With this cumulative process, the last element in $\mathbf{B}$ effectively depends on all prior points.

The quality of this concept is linked to the point spread function. An ideal coil would have a Dirac delta function, so $PSF_n = 0$ for $n \neq 0$. In this case $\mathbf{S}'$ would be a diagonal matrix, with a trivial inverse. For the sensitivity function in Eqn. 2.11, the point spread function is constant for a certain length, so $PSF_n = c$ for $n = 0, 1, \cdots, M-1$. This hard edge model still is not a precise description of the true sensitivity function. Due to the multiple windings, the function has a finite growth rate and therefore a continuous edge, see Fig. 5.1 for the three models.

A way to classify the robustness to perturbations of linear algebraic systems is the condition number [27]. We tested the three point spread functions from Fig. 5.1 for the condition number of their corresponding matrix $\mathbf{S}'$ - the results are summarized in Table 5.1. As expected the ideal coil is perfectly conditioned. The more precise model on the other hand, almost doesn't allow to solve the problem at all. This observation also manifested on some trials with test data. We want to point out a specific problem observed with the hard edge model. In the deconvoluted data appears a strong oscillation. Its fundamental

Point spread function	Condition number of $\mathbf{S}'$
Dirac delta	1
Hard edge	6.45×10^3
Continuous edge	9.35×10^{10}

Table 5.1: The condition number of $\mathbf{S}'$ is affected by the point spread function. The matrix $\mathbf{S}'$ was set up with $L = 5000$ and the point spread function according to Fig. 5.1.

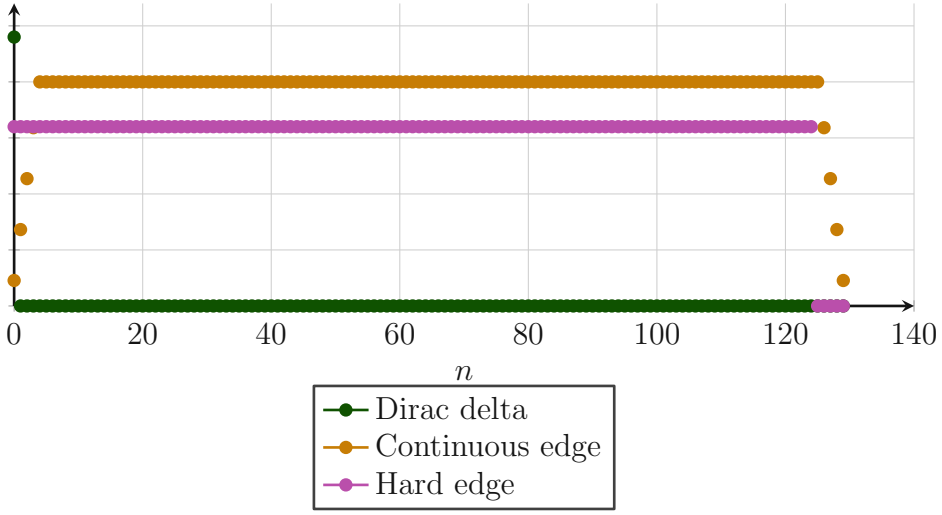

Figure 5.1: Three different models of the point spread function. Amplitudes are scaled individually for better representation.

component corresponds with the length of the point spread function. A coil with a infinite small edge would be blind for all sinusoidal components multiple of the coil's length. In the reconstruction those components appear to be prone for instabilities.

5.1.2 Frequency Domain

As commonly known, a convolution in time domain corresponds to a multiplication of the two involved spectra. So we write the corresponding problem description in frequency domain as

$$\mathscr{F}\{\Phi_n\} = \mathscr{F}\{B_n * PSF_n\} = B(f)PSF(f) = \Phi(f). \tag{5.5}$$

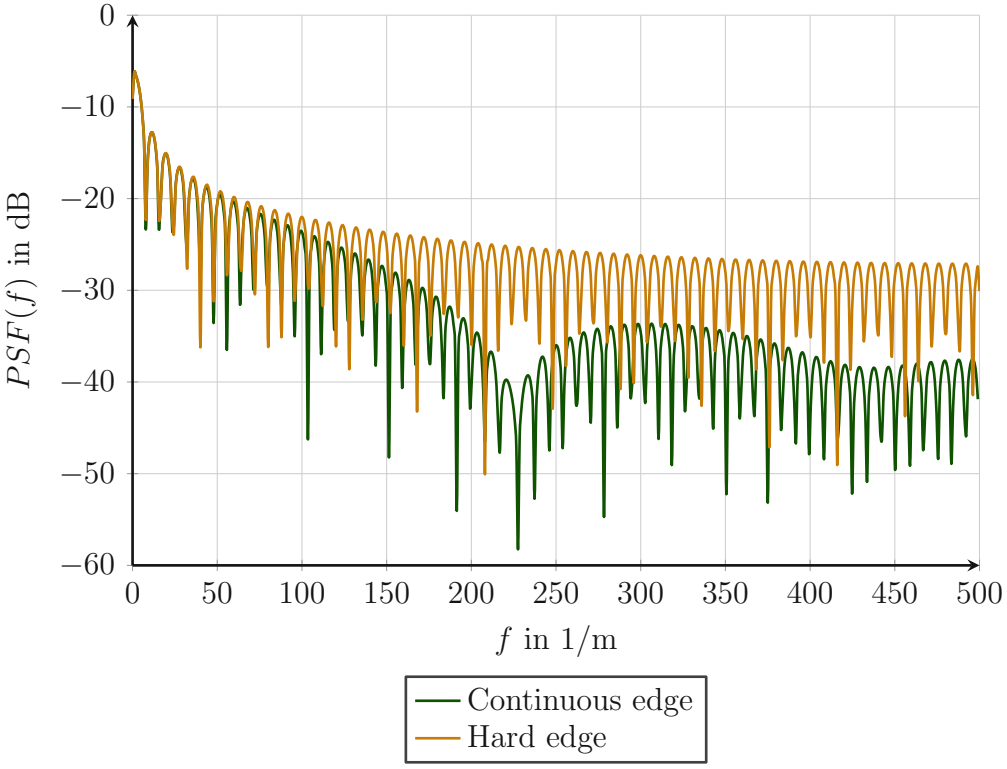

Figure 5.2: Both hard and continuous edge model exhibit regular minima, which amplify the measurement noise at these frequencies.

For $PSF(f)$ we use the PSFs from Fig. 5.1 and perform a Fourier transform, see Fig. 5.2.

Following the approach from [28], we want to find a filter $g(f)$ that forms the inverse of the point spread function. With a simple approach $g(f) = 1/PSF(f)$ we only have success for a noise-free measurement signal. A noise afflicted signal is amplified at frequencies where $PSF(f)$ is small. The Wiener-Kolmogorov filter tackles this problem by multiplying a damping factor which depends on the signal-to-noise ratio $SNR(f)$ to minimize the expected mean-squared error in the frequency domain

$$g(f) = \frac{1}{PSF(f)} \frac{|PSF(f)|^2}{|PSF(f)|^2 + \frac{\mathbb{E}\left[n(f)\right]^2}{\mathbb{E}\left[B(f)\right]^2}}. \tag{5.6}$$

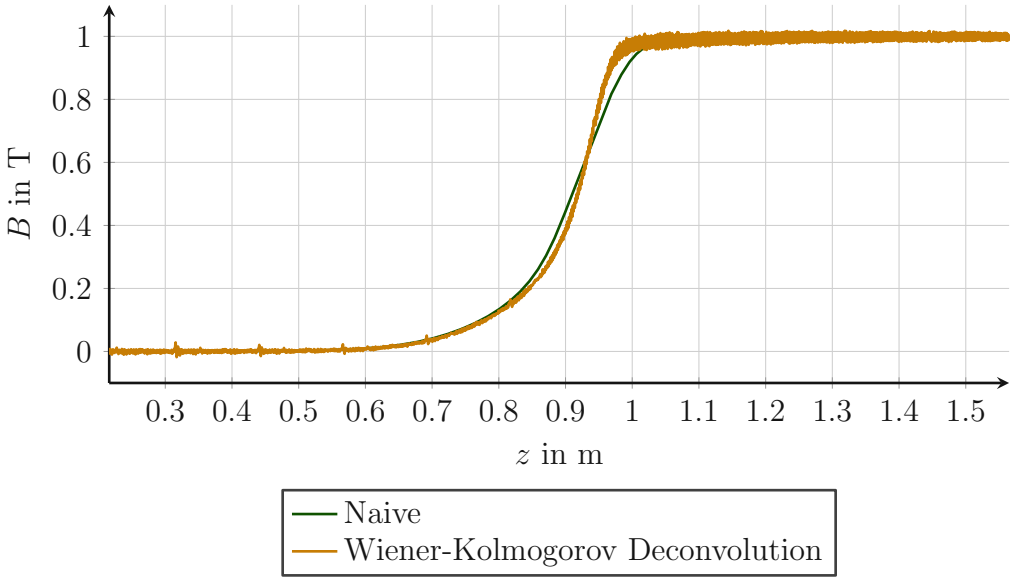

Figure 5.3: Comparison between the naive "deconvolution" and the Wiener-Kolmogorov deconvolution shown in the pole's end region. For this graphic we used the continuous edge model for PSF.

For the power density spectrum of the noise $n(f)$ and $B(f)$ we only can make assumptions. To estimate the quality of this approach we used the measurement data from Sec. 4.2. We used the averaged results from Fig. 4.6 as noise free signal. As noise we use the point-wise difference between the actual measurement signal and the averaged signal. On these results we performed a fast Fourier transform, which gives us an estimation of $SNR(f)$. Of course this is only an estimation because we use the convoluted signal as approximation for the deconvoluted signal.

Our studies show that the results are not satisfactory. The deconvoluted B looks very noisy, see Fig. 5.3. At the end regions we see an expected effect of the convolution - it protracts the steep rise of the field. In the frequency domain it becomes visible that we have strong oscillations at the harmonics where $PSF(f)$ is small, see Fig. 5.4.

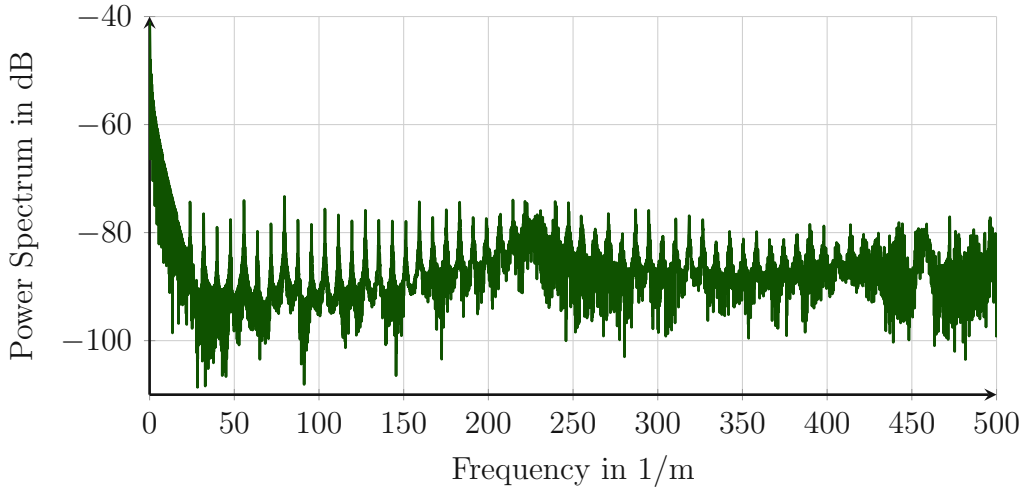

Figure 5.4: The spectrum of the Wiener-Kolmogorov deconvoluted field B. The continuous edge model was used for these calculations, compare to Fig. 5.2.

5.1.3 Basis Splines

In the previous section we expressed B in the frequency domain. In a more general description we write

$$B(z) = \sum_{k=1}^{K} a_k \varphi_k(z), \tag{5.7}$$

to expand B into basis functions $\varphi_k(z)$. We have the freedom to choose any type of basis functions, for example sinusoidal functions for Fourier transformation. We insert Eqn. 5.7 into Eqn. 2.12

$$\Phi_n = \sum_{k=1}^{K} a_k \int_{-\infty}^{\infty} s(z' - z_n)\varphi_k(z')\,\mathrm{d}z'. \tag{5.8}$$

Using $\mathbf{a} = (a_1, \ldots, a_K)$ and a matrix $\mathbf{D}$ with its entries

$$[\mathbf{D}]_{n,k} = \int_{-\infty}^{\infty} s(z' - z_n)\varphi_k(z')\,\mathrm{d}z' \tag{5.9}$$

we get the equation system

$$\mathbf{\Phi} = \mathbf{D}\mathbf{a}. \tag{5.10}$$

Solving the deconvolution problem gets down to find a solution for $\mathbf{a}$ [25].

The choice of the basis functions $\varphi_k(z)$ is critical for the stability of the inverse problem. The underlying differential equations would suggest a Fourier basis $\varphi_n(z) = \exp(-2\pi j/n)$. As we showed above, such a basis causes problems for long sensitivity functions [28]. Therefore we make use of basis splines of third order as suggested in [25].

Once we found a solution to Eqn. 5.10 for a given discretization, we can reconstruct the flux with Eqn. 5.8 to obtain Φ_n^{R}. The residuals $\Phi_n^{\mathrm{R}} - \Phi_n$ are used as criterion for further refinement. Practice showed that the approximation depends strongly on the number of knots. Whereas the goodness of the fit does not strictly improve with a higher number of knots. When the number becomes too big, we introduce oscillations. Therefore we use an adaptive refinement, based on the residuals. We started the algorithm with 7 equally long intervals. Practice proofed that it is reasonable to stop the refinement when the residuals are below a few $10^{-5}\,\mathrm{V\,s}$, see Fig. 5.5 for the result of the central coil.

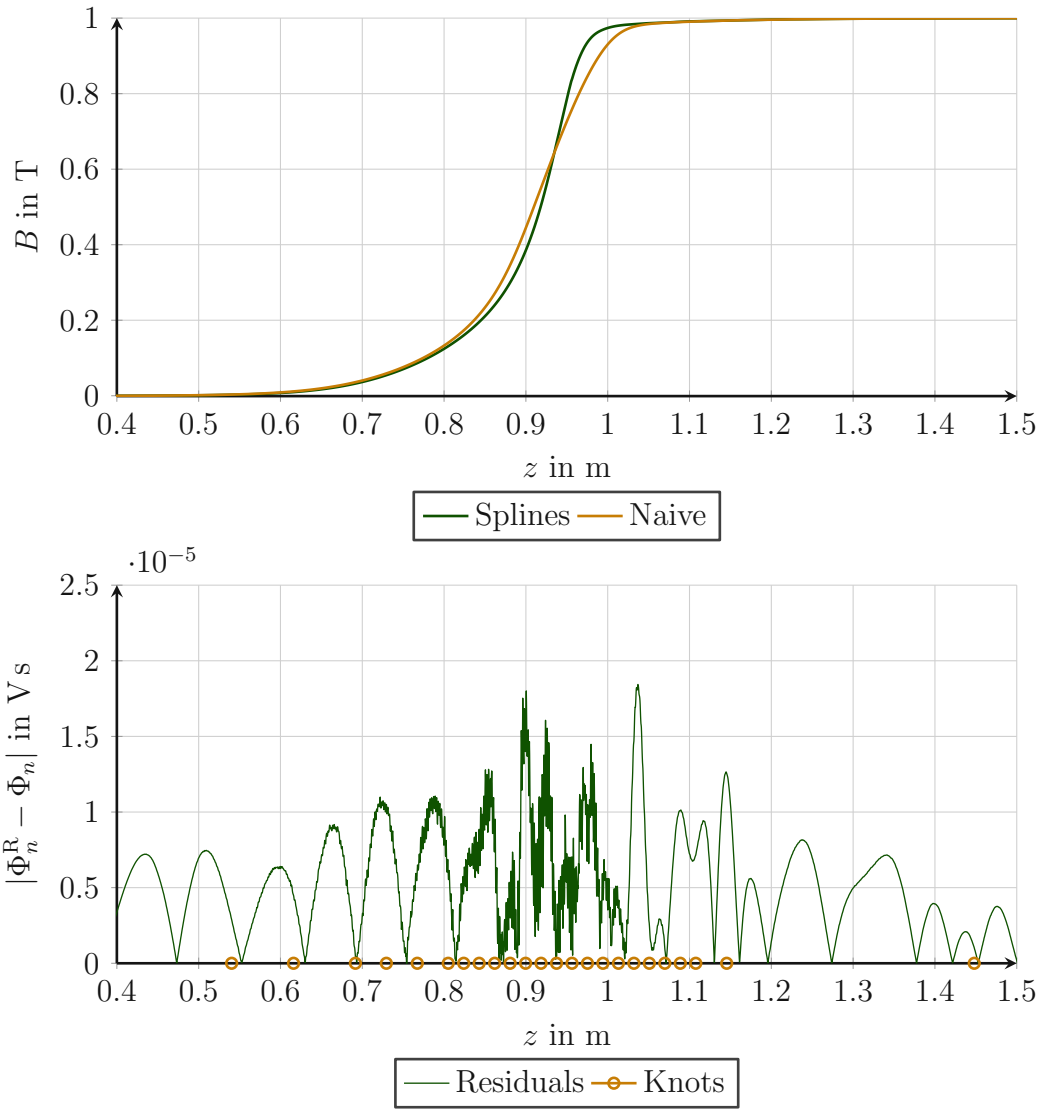

Figure 5.5: Using cubic B-splines as basis function gives a smooth deconvoluted field B. The knots are tightend in areas of a strong field change.

5.2 Pseudo Multipoles

The 2D field harmonics (multipole coefficients) are suitable to describe integrated fields. Their solution is based on a Fourier series and don't have any dependency on the z coordinate [5].

To describe the field distributions in the end regions of a magnet we use coefficients of a Fourier-Basel series, known as pseudo-multipoles [28]. A description for those coefficients is found by consequently solving the Laplace equation in cylindrical coordinates for the magnetic scalar potential ϕ_m

$$\Delta\phi_\mathrm{m} = \frac{1}{r}\frac{\partial}{\partial r}\left(\frac{r\partial\phi_\mathrm{m}}{\partial r}\right) + \frac{1}{r^2}\frac{\partial^2\phi_\mathrm{m}}{\partial\varphi^2} + \frac{\partial^2\phi_\mathrm{m}}{\partial z^2} = 0 \quad ; \tag{5.11}$$

as shown in [29] and [30]. We make use of the method of separation of variables $\phi_\mathrm{m}(r,\varphi,z) = R(r)\phi(\varphi)Z(z)$ and write the Laplace equation as

$$\frac{1}{Rr}\frac{\mathrm{d}R}{\mathrm{d}r} + \frac{1}{R}\frac{\mathrm{d}^2R}{\mathrm{d}r^2} + \frac{1}{\phi r^2}\frac{\mathrm{d}^2\phi}{\mathrm{d}\varphi^2} = -\frac{1}{Z}\frac{\mathrm{d}^2Z}{\mathrm{d}z^2}. \tag{5.12}$$

We introduce the following solutions

$$Z(z) = \begin{Bmatrix}\cos\, pz\\ \sin\, pz\end{Bmatrix}, \tag{5.13}$$

$$\phi(\varphi) = \begin{Bmatrix}\cos\, n\varphi\\ \sin\, n\varphi\end{Bmatrix}, \tag{5.14}$$

$$R(r) = I_n(pr) \tag{5.15}$$

where $I_n(pr)$ is the modified Bessel function with $p > 0$. The curly braces indicate the linear combination of its arguments. The solutions are adapted to boundary conditions given by real world limitations [30].

We build the linear combination of all possible solutions. Then following the derivation in [29] and [30], we obtain an expression for the magnetic scalar potential

$$\phi_\mathrm{m}(r,\varphi) = \sum_{n=1}^{\infty} r^n \left(\widetilde{C}_n(r,z)\sin n\varphi + \widetilde{D}_n(z)\cos n\varphi\right), \tag{5.16}$$

where

$$\widetilde{C}_n(r,z) = C_{n,n}(z) - \frac{C^{(2)}_{n,n}(z)}{4(n+1)}r^2 + \frac{C^{(4)}_{n,n}(z)}{32(n+1)(n+2)}r^4 - \cdots,$$
$$\widetilde{D}_n(r,z) = D_{n,n}(z) - \frac{D^{(2)}_{n,n}(z)}{4(n+1)}r^2 + \frac{D^{(4)}_{n,n}(z)}{32(n+1)(n+2)}r^4 - \cdots. \tag{5.17}$$

In opposite to the 2D field harmonics, these coefficients don't exhibit a pure r^{n-1} dependency. For fields with a small variation in z, the derivatives go to zero and the coefficients become identical to the 2D field harmonics [30].

We obtain the field components by

$$B_r = -\mu_0 \frac{\partial \phi_\mathrm{m}}{\partial r}, \qquad B_\varphi = -\mu_0 \frac{1}{r}\frac{\partial \phi_\mathrm{m}}{\partial \varphi}, \qquad B_z = -\mu_0 \frac{\partial \phi_\mathrm{m}}{\partial z}. \tag{5.18}$$

For now we have a special interest in B_φ

$$B_\varphi(r,\varphi,z) = -\mu_0 \sum_{n=1}^{\infty} n r^{n-1} \left(\widetilde{C}_n(r,z)\cos n\varphi - \widetilde{D}_n(r,z)\sin n\varphi\right). \tag{5.19}$$

Now we want to transform Eqn. 5.19 from a cylindrical to a Cartesian coordinate system, following [30]. To obtain the field component in $\mathbf{e}_y$ from cylindrical coordinates we use

$$\mathbf{B}\cdot\mathbf{e}_y = B_\mathrm{y} = B_r \sin\varphi + B_\varphi \cos\varphi. \tag{5.20}$$

For B_y in the plane $y = 0$, so $\varphi \in \{0, \pi\}$, we find the expression

$$B_\mathrm{y} = \cos\varphi \sum_{n=1}^{\infty} n r^{n-1} \widetilde{C}_n(r,z)\cos(n\varphi), \tag{5.21}$$

where we omitted the skew components $\widetilde{D}_n$. With $y = 0$ and $\varphi \in \{0, \pi\}$ we get $r = x/\cos\varphi = |x|$ and further

$$B_\mathrm{y} = \sum_{n=1}^{\infty} n \underbrace{|x|^{n-1}\cos\varphi\cos(n\varphi)}_{(1)} \widetilde{C}_n(|x|,z). \tag{5.22}$$

Instead of (1) we can directly write x^{n-1}. The coefficients $\widetilde{C}_n(r,z)$ can directly be written as $\widetilde{C}_n(x,z)$. So we finally obtain

$$B_\mathrm{y}\left(x, y=0, z\right) = \\ -\mu_0 \sum_{n=1}^{\infty} n x^{n-1} \left(C_{n,n}(z) - \frac{C^{(2)}_{n,n}(z)}{4(n+1)} x^2 + \frac{C^{(4)}_{n,n}(z)}{32(n+1)(n+2)} x^4 - \cdots \right). \quad (5.23)$$

When we truncate the sum at $n = 7$ and the 6th derivative, we obtain the approximation

$$\begin{aligned} \frac{-1}{\mu_0} B_\mathrm{y}\left(x, y=0, z\right) \approx \\ & x^0 \left(1 C_{1,1}(z)\right) \\ & x^1 \left(2 C_{2,2}(z)\right) \\ & x^2 \left(3 C_{3,3}(z) - \frac{C^{(2)}_{1,1}(z)}{8}\right) \\ & x^3 \left(4 C_{4,4}(z) - \frac{2 C^{(2)}_{2,2}(z)}{12}\right) \\ & x^4 \left(5 C_{5,5}(z) - \frac{3 C^{(2)}_{3,3}(z)}{16} + \frac{C^{(4)}_{1,1}(z)}{192}\right) \\ & x^5 \left(6 C_{6,6}(z) - \frac{4 C^{(2)}_{4,4}(z)}{20} + \frac{2 C^{(4)}_{2,2}(z)}{384}\right) \\ & x^6 \left(7 C_{7,7}(z) - \frac{5 C^{(2)}_{5,5}(z)}{24} + \frac{3 C^{(4)}_{3,3}(z)}{640} - \frac{C^{(6)}_{1,1}(z)}{9216}\right). \end{aligned} \quad (5.24)$$

This is a polynomial series expansion at each z [30]

$$B_\mathrm{y}\left(x, y=0, z\right) = \sum_{n=1}^{7} C_n(z) x^{n-1}. \quad (5.25)$$

The coefficients $C_n(z)$ are found by a polynomial fit of the measurement data, see Fig. 5.6. With the current setup we have 13 tracks for the fit available. We will discuss the influence of the choice of the included coils further below.

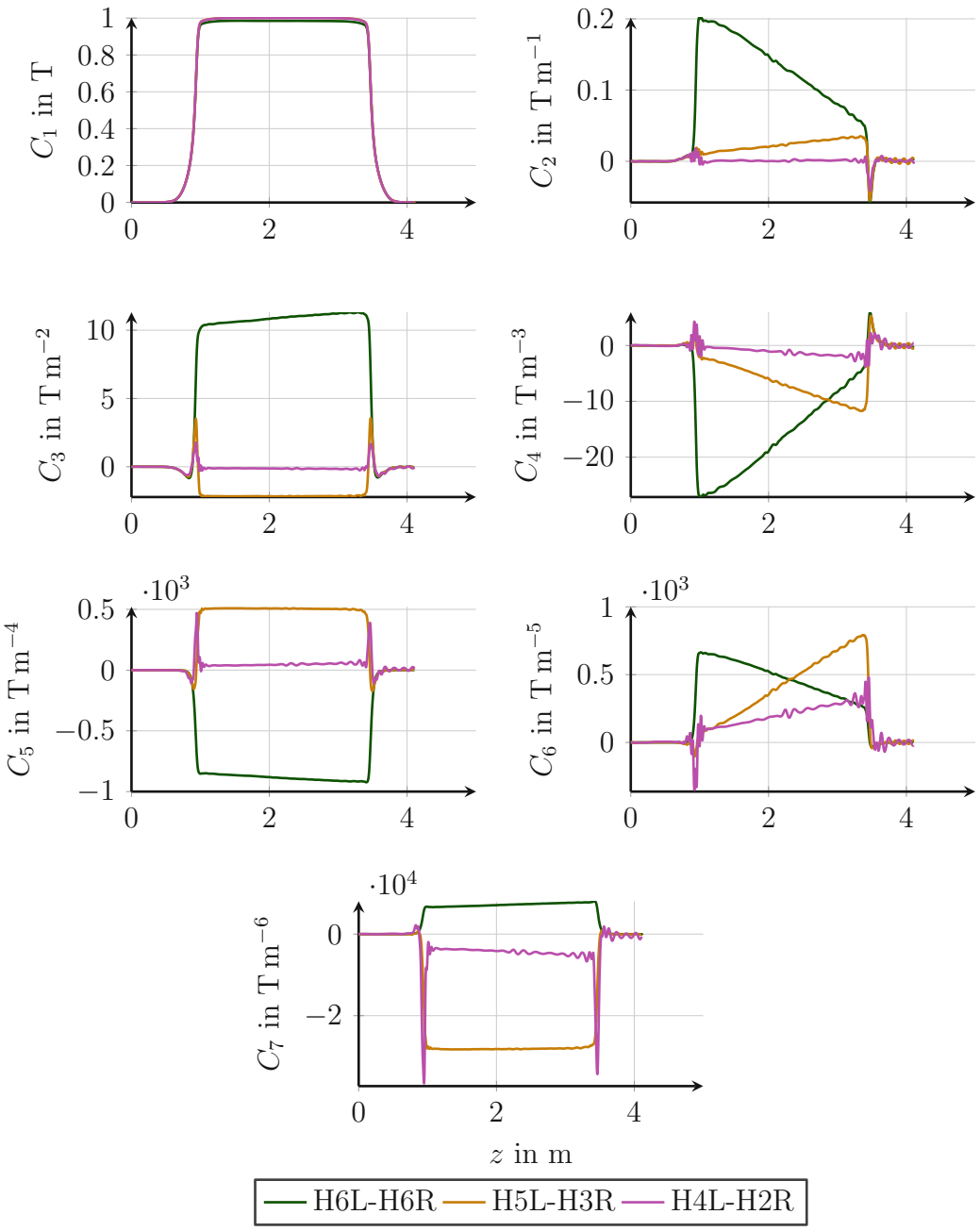

Figure 5.6: For each z we fit a 7th order polynomial to the measurement data to find the coefficients $C_n(z)$. We used three different set of tracks for these fits, with 13 (—), 9 (—) and 7 (—) coils.

By comparing Eqn. 5.24 with Eqn. 5.25 we find the multipoles $C_{n,n}$. For $n = 1$ we can extract

$$C_1(z) = -\mu_0 C_{1,1}(z) \tag{5.26}$$

and directly use the second deviation of $C_{1,1}$ for $n = 3$

$$C_3(z) = -\mu_0 \left(3C_{3,3}(z) - \frac{C_{1,1}^{(2)}(z)}{8} \right). \tag{5.27}$$

With this iterative process we find all coefficients $C_{n,n}$ up to the order $n = 7$, see Fig. 5.7.

We use two major approximations for this process. First, we truncate the series in Eqn. 5.23. As we truncate higher order terms and also limit the derivation, we suppress higher order measurement uncertainties. This already manifests in the polynomial coefficients $C_n(z)$. Second, we need to smooth our data in z. This smooth is necessary because we use measurement data and want to obtain up to the 6th derivative. Numerical differentiation is very sensitive to noise and tends to overshoot. The situation is slightly relaxed, as we deconvoluted using splines, so B_y is given as a cubic spline. This assures a differentiability up to the third derivative. Since this is still not enough we apply smoothing splines[1] on the data after each derivative. This allows to control the smoothness with a single parameter. With smoothing we typically loose information, especially on sharp peaks, which are prone to appear with higher derivatives.

Coefficients in Fig. 5.6 and Fig. 5.7 are calculated for different sets of coils. The choice of coils has an high impact on the first approximation - the goodness of the fit. When we use only the most inner coils H4L - H2R, the fit reduces to finding a unique solution, so we have no deviation between the data and the fit. By reducing the set of coils to the more central ones, we cover only the homogeneous region, where we have a symmetric field distribution and therefore decreased even components $C_{2n,2n}$. A larger set of coils cover the unsymmetrical field (recall that we measured in a C-shaped magnet) and therefore produce even components. Keep in mind that in our case, a larger number of coils means a larger transversal space that we cover. For smaller set, we can observe some oscillations. These are artifacts from the deconvolution and are smoothed away for larger amount of coils by the polynomial fit.

[1] `https://de.mathworks.com/help/curvefit/smoothing-splines.html`

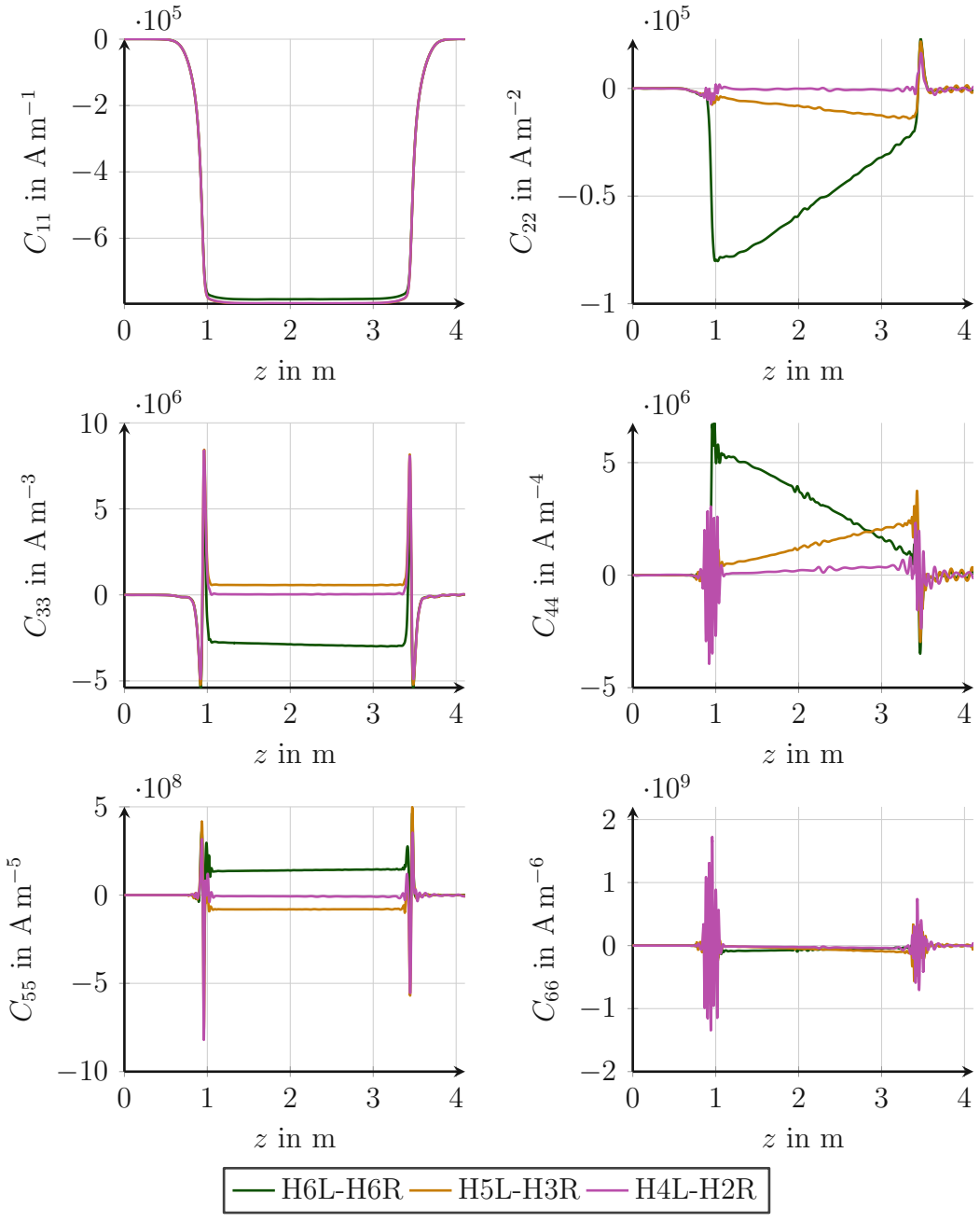

Figure 5.7: With the iterative process we find the coefficients $C_{n,n}(z)$ of the pseudo multipoles using the coefficients $C_n(z)$. They vary on the choice of the included coils.

Based on studies that we depicted in Fig. 5.7, we came to the awareness that the pseudo multipole decomposition is intended for cylindrical apertures. To get a 3D representation of the field, one needs to limit the evaluation to an artificial cylindrical structure that fits in the aperture, since the derivation of the pseudo multipoles is based on the Laplace equation. This requires to have a source free domain, which is afflicted when we try to inscribe a cylinder with $r > H$, where H is the height of the pole. For our setup, we could include maximum 3 coils for the pseudo coefficient extraction.

With the pseudo multipoles that we extracted from a single plane, we should be able to reconstruct the field at any point of the magnets aperture. We compared the reconstructed field B^{r} with the measured field B^{m} at two further planes where we have measurements available, see Fig. 5.8. For these results, we extracted the multipole coefficients using the 7 most inner coils H4L - H2R. For the field reconstruction outside of the plane $y = 0$ we need to consider the radial component B_r as well. Using Eqns. 5.18 and 5.20, as well as results from [30] we can express B_{y} as

$$-\frac{B_{\mathrm{y}}}{\mu_0} = \sin\varphi \sum_{n=1}^{\infty} r^{n-1}\overline{C}_n(z)\sin(n\varphi) + \cos\varphi \sum_{n=1}^{\infty} n r^{n-1}\widetilde{C}_n(z)\cos(n\varphi) \quad (5.28)$$

with

$$\overline{C}_n = nC_{n,n}(z) - \frac{(n+2)C^{(2)}_{n,n}(z)}{4(n+1)}r^2 + \frac{(n+4)C^{(4)}_{n,n}(z)}{32(n+1)(n+2)}r^4 - \cdots \quad (5.29)$$

The difference $B^{\mathrm{r}} - B^{\mathrm{m}}$ ranges in the same order of magnitude as the difference $B^{\mathrm{m}}(y=0) - B^{\mathrm{m}}(y=y_0)$. With larger distances the error on the approximations seems to become more evident. The strong dependency of r in Eqn. 5.28 also suggests this observation.

Another interesting point to consider is the influence of the deconvolution using splines. We compared the pseudo multipoles $C_{n,n}$ calculated using the naive deconvoluted field and using the spline-deconvoluted field, see Fig. 5.9. We observe that the spline deconvoluted field is somewhat steeper, which depicts for example in $C_{3,3}$ in sharper peaks. Also the smoothness of the spline deconvoluted field is visible in $C_{6,6}$. In constant field regions the effect of the spline deconvolution is small apart from the smoothing effect.

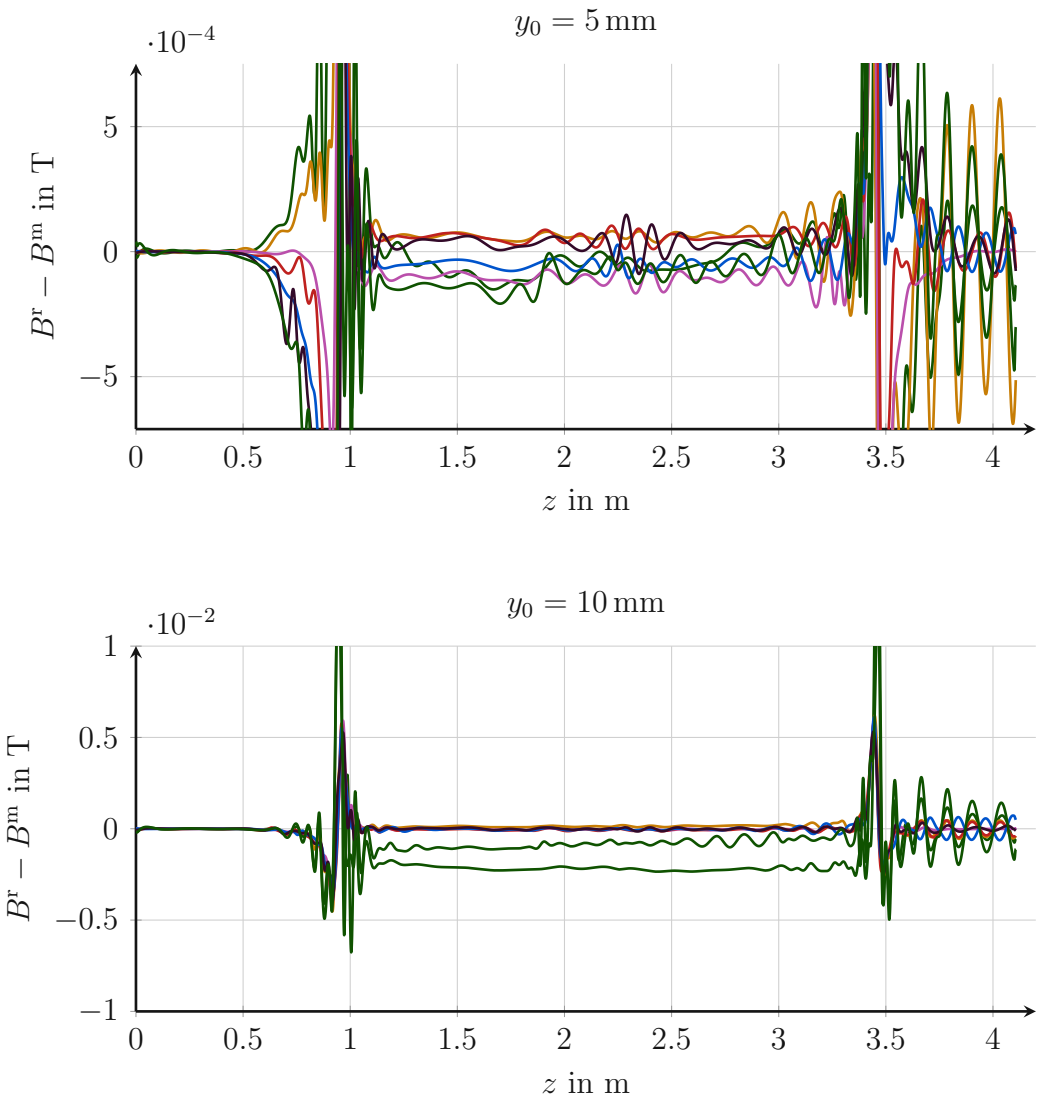

Figure 5.8: The coefficients $C_{n,n}(z)$ are used to calculate the field at other planes y_0. This reconstructed field $B^{\mathrm{r}}(y = y_0)$ is compared to the field measured at the same planes $B^{\mathrm{m}}(y = y_0)$ at various tracks.

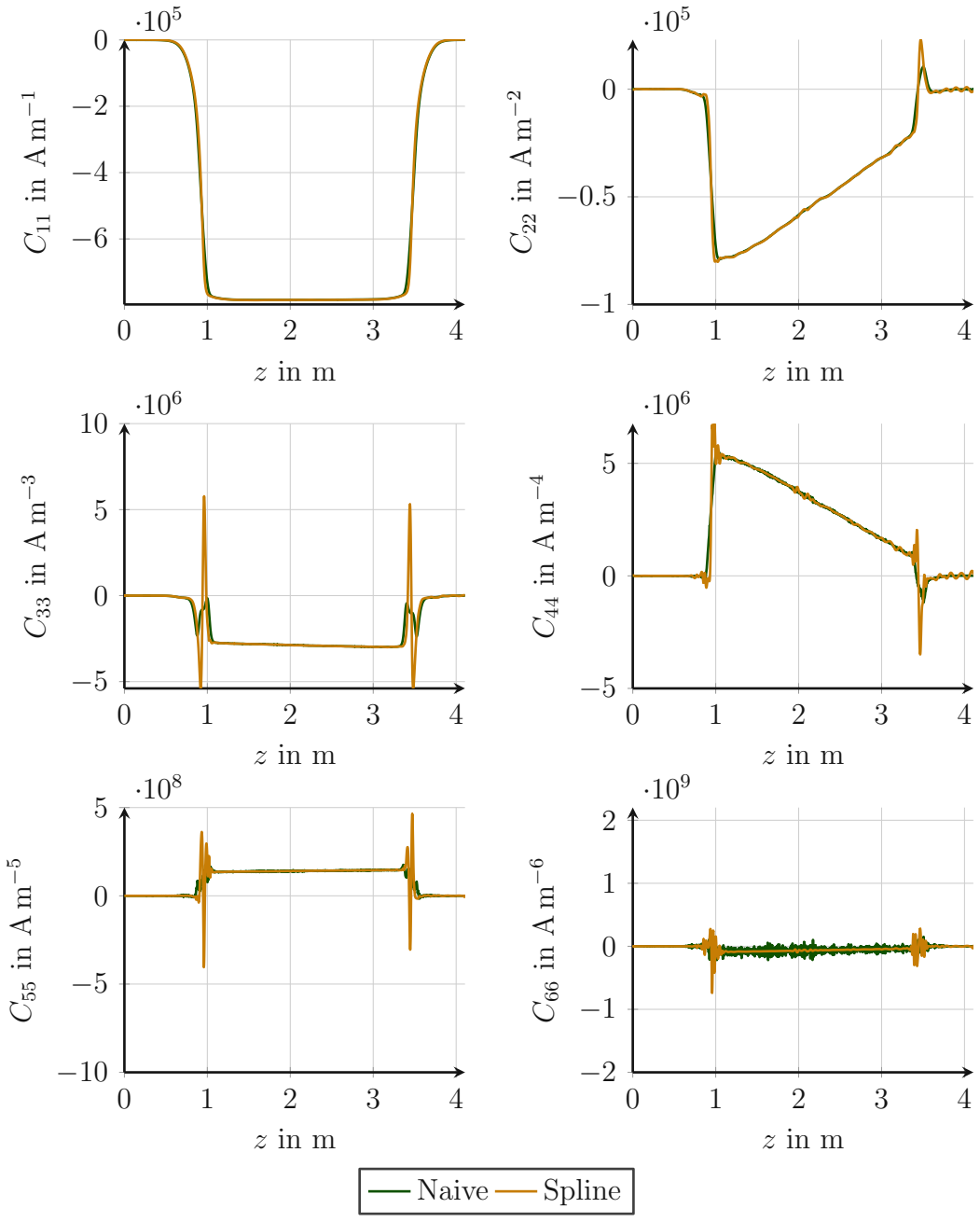

Figure 5.9: The deconvolution methods manifest in the pseudo multipole coefficients $C_{n,n}(z)$.

6 Critical Reflection and Outlook

The translating fluxmeter gives a new insight to the local field distribution. With a longitudinal field profile researchers have a powerful tool for the studies of accelerator magnets. Our studies exhibit in general an excellent result. Nevertheless, we can determine open points for further studies and potential improvements for a follow up device.

From Chapter 5 we know the importance and difficulty of the deconvolution. We saw that the sensitivity function has a strong effect on the solution of the inverse problem. From the study of the Wiener-Kolmogorov deconvolution filter we temp to want a sensitivity function without points close to zero. This would result in a infinite spread spectrum. The corresponding function in the spatial domain would in general need to be infinite small according to the Fourier bandwidth theorem. An alternative is a Gauss function. This approach is currently in progress and first studies show promising results [31]. There is a certain freedom in the coil design, because we could show that we have an excellent signal. So a reduction in the effective coil surface would still give us a high signal to noise ratio - in certain limits.

Further studies should be done for the pseudo multipole decomposition. One can think of scenarios where the limitation $r < H$ can be insufficient. Anyway, for evaluations in the measurement plane only, an interpolation between the coils can be sufficient. In a future step, measurements can be acquired at several layers and/or on the boundaries. These results can be further used to create a BEM/FEM model.

During our metrological characterization campaign we experienced the importance of the mechanics. On one hand, the user needs to take care of a solid and flat support for the device. The positioning of the device in correspondence with the magnet can be labor-intensive when there is no position for the laser tracker to see all reference points of the plate. On the other hand, the moving parts need to be well aligned, in order to prevent extra vibrations. Our studies showed that

the cable chain is one source of the vibrations. With extra studies one could determine and resolve further sources of vibrations. Equipping the carriage with an acceleration sensor, can give an insight in the modes of vibration.

One of the most delicate mechanical parts of the translating fluxmeter is the encoder strip. A single scratch can require the change of the entire strip. This is not only connected with the high costs of the strip itself, but also with the involved work of mounting and recalibrating the encoder as well as the offset between go and return run. During an ongoing measurement campaign, this could be a critical time loss. Considering the delicateness of the strip, it is venturesome not to have any kind of protection. During the work with the translating fluxmeter, we also experienced some problems with dust and other small soil on the strip. Since the strip is placed facing upwards without any protection, this is prone to happen. For future designs we therefore recommend to place the strip at least side ways and include a protection mechanism. To get rid of dust, a brush or similar could be directly mounted to the carriage.

In Sec. 3.1.2 we showed that the compensation requires us to consider the entire electrical measurement network. A cross talk between both coils is inevitable when we use a compensation. We recommend to review the effects of a compensation in our specific setup and weight it up against the uncertainty that we obtain from the shared electrical network.

The offset between the go and the return run could be removed by adapting the hardware. This decreases the calibration procedure as well as the post processing effort. In order to achieve that, we assume that the device only is used with complete cycles, meaning a go run is always followed by a return run. In practice this proved to be valid, so we can remove the second index marker. With some modifications on the firmware of motor controller and the encoder board, we generate the triggers based on the counting of the encoder board. This is achievable using the direction of movement. Removing the second index marker has a positive side effect for the encoder. Since this is the indented way of operation, it can detect the index marker a bit more reliable.

Our metrological measurement campaign exhibited promising results. A further study can be launched for the influence of the velocity. While we expect the results to be completely independent from the target velocity, we still observed a minor effect.

7 Summary

Driven by the requirements of the magnetic measurement actions for the Super-FRS dipoles, a concept for the translating fluxmeter was developed. A proof of principle was already accomplished with a prototype. Based on those experiences a more elaborated device was designed. Apart from the application oriented use of the translating fluxmeter, it can give interesting insights in research oriented questions.

For the modeling we started the derivation at the Faradys law. This revealed that voltage induced in the coil is linked to the field at the rim of the coil and the velocity. We use an integrator to digitize the induced voltage and output it as flux. A trigger tells the integrator to output the current value and reset the integration to zero. In order to be independent from the velocity, we use a linear encoder with a high resolution. The encoder generates a spatial trigger and hands it to the integrator. Mathematically this is described as reparametrization from time to space.

Consequently following the idea to find a link between the wanted field and the induced voltage, we concluded that a convolution can describe this link. Also from a practical point of view, it becomes obvious that the sensitivity function is a crucial part. We showed that the deconvolution is not relevant for the calculation of the total integral. To obtain a correct field profile, it becomes more important. Although we have a high SNR, the noise shows to be problematic with known deconvolution methods. To facilitate finding a solution of the inverse problem, one needs to dedicate special attention to the coil design. We succeeded finding a satisfying solution using B-splines. Oscillations that we saw in the frequency domain, are well controlled with B-splines.

We used the data acquired at the central plane, to extract pseudo multipole coefficients for the reference dipole. It showed that we need to limit the amount of coils included, otherwise we conflict the primary assumption to the pseudo multipoles of a source free domain.

After a close look at the system design, we could seek out various systematic corrections. Variables that show up directly in the modeling process are the effective coil surface and the field offset at the starting position. Based on well-known techniques, we calibrated the coil surface in a reference dipole. This was done to proof the validity of the designed value. For the field offset we added a hall sensor to measure the local field at the starting point.

Additionally we need to systematically correct for non ideal properties of used devices, headed up by the integrators. First we need to correct for the electrical measurement network. Due to the compensation, the results of the absolute and the compensated coils are affected by each other. Being a linear network, we could correct this with calibrated values. Secondly, we have an offset on the ADC of the integrator. This manifests in a drift. A first order correction is done for each cycle independently. Additionally we need to consider an offset between the go and the return run. This requires a calibration procedure to obtain those offsets.

We used a reference dipole magnet to verify the results from the translating fluxmeter. We analyzed mechanical properties of the device with a laser tracker. When the translating fluxmeter is handled as specified, no major non-reversible deformation could be observed. The current device has some minor vibrations, that carry forward to the flux measurement on a very low scale.

A measurement with fixed parameters and field, revealed that the translating fluxmeter has a very low standard deviation. Varying the parameters from measurement to measurement showed us the sensibility of the system to those parameters. The nominal velocity exhibited an effect on the results, but in a minor range. We determined optimized values for the device parameter.

We accomplished a widespread analysis of the translating fluxmeter. Our characterization campaign didn't reveal any significant deviation that would increase the measurement uncertainty. But there are open points that need additional studies for a further improvement of the system. The translating fluxmeter proofed to be a powerful measurement device for applied measurements.

Appendix

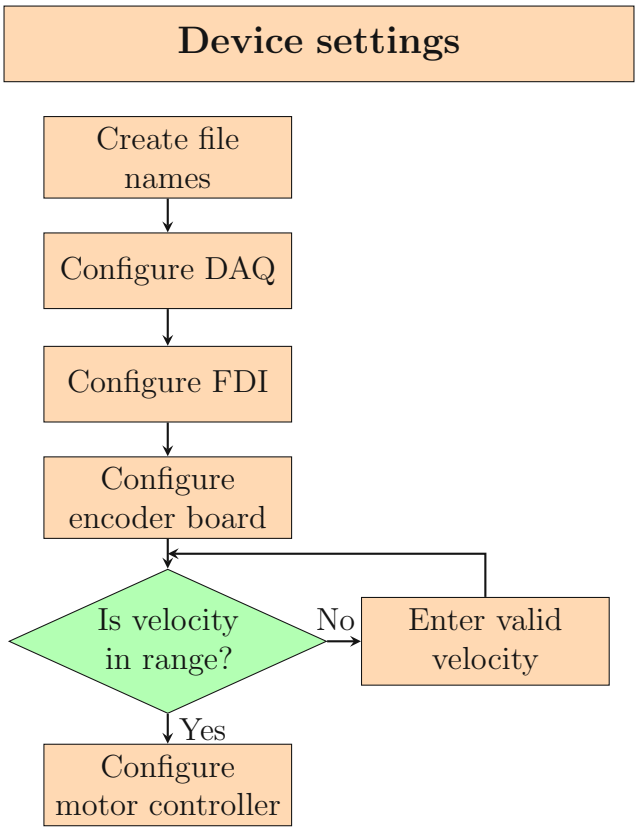

Figure A.1: Device Settings

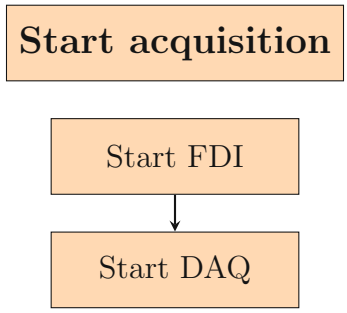

Figure A.2: Start Acquisition

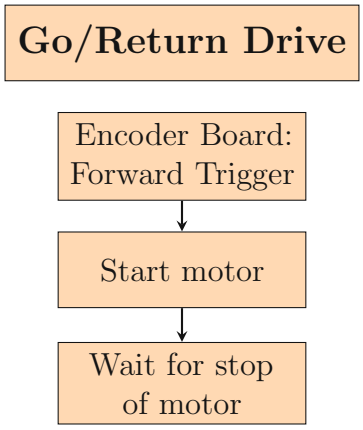

Figure A.3: Go/Return Drive

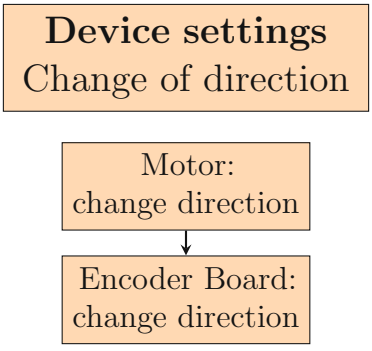

Figure A.4: Device settings - Change of direction

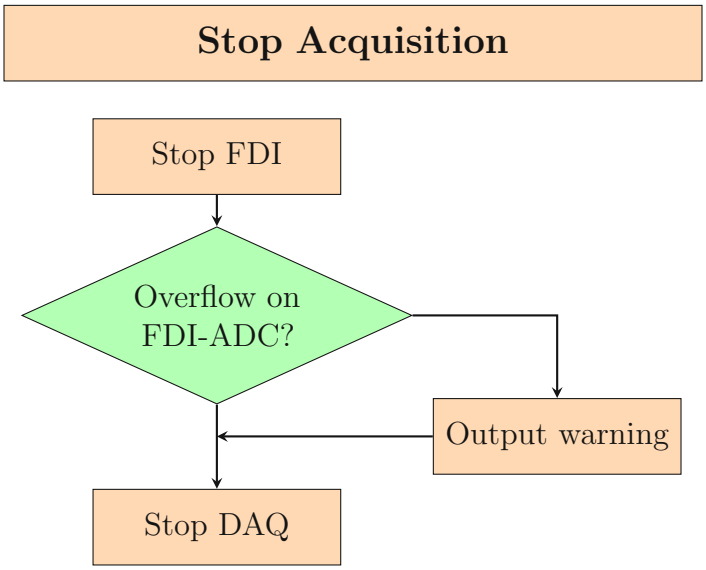

Figure A.5: Stop Acquisition

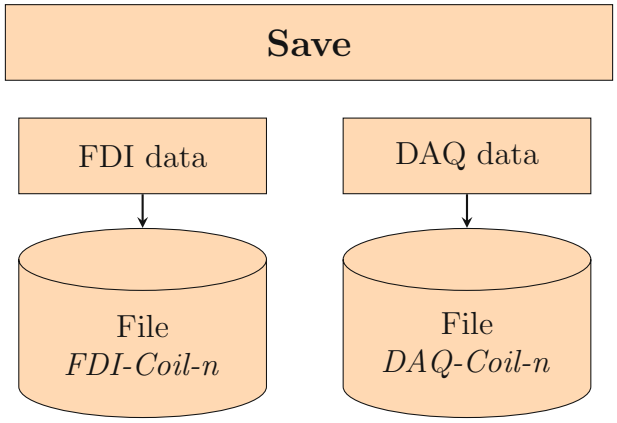

Figure A.6: Device settings - Change of direction

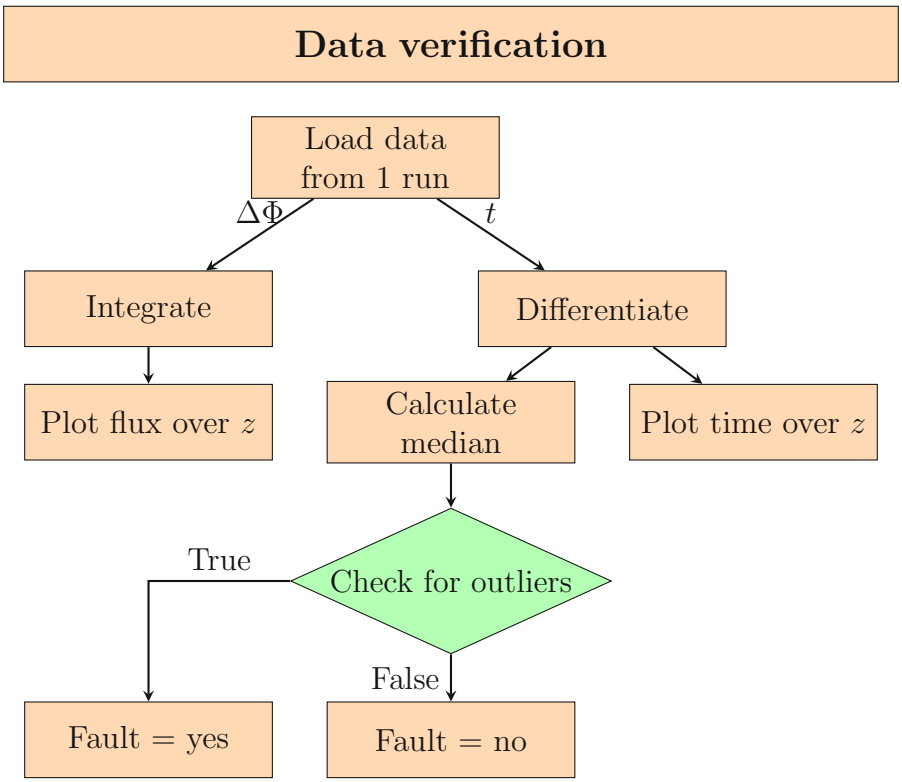

Figure A.7: Stop Acquisition

Bibliography

[1] L. Bottura and K. N. Henrichsen. "Field Measurements." In: *CAS - CERN Accelerator School : Superconductivity and Cryogenics for Accelerators and Detectors* (2002). DOI: 10.5170/CERN-2004-008.118.

[2] J. DiMarco et al. "Field alignment of quadrupole magnets for the LHC interaction regions." In: *IEEE Transactions on Applied Superconductivity* (2000).

[3] Carlo Petrone. "Wire methods for measuring field harmonics, gradients and magnetic axes in accelerator magnets." 2013.

[4] L. Walckiers. *Magnetic measurement with coils and wires*. 2011. arXiv: 1104.3784 [physics.acc-ph].

[5] Stephan Russenschuck. *Field computation for accelerator magnets: analytical and numerical methods for electromagnetic design and optimization*. 2011.

[6] A. K. Jain. "Harmonic coils." In: *CAS - CERN Accelerator School : Measurement and Alignment of Accelerator and Detector Magnets* (1998). DOI: 10.5170/CERN-1998-005.175.

[7] M. Buzio. "Fabrication and calibration of search coils." In: (2011). DOI: 10.5170/CERN-2010-004.387.

[8] G. Golluccio et al. "PCB coil array for measuring curved accelerator dipoles: two case studies on the MedAustron accelerator." In: *Proceedings of IMEKO 2014* (2014).

[9] M. Winkler et al. "The status of the Super-FRS in-flight facility at FAIR." In: *Nuclear Instruments and Methods in Physics Research Section B: Beam Interactions with Materials and Atoms* (2008). DOI: 10.1016/j.nimb.2008.05.073.

[10] H. Leibrock et al. "Prototype of the superferric dipoles for the Super-FRS of the FAIR-project." In: *IEEE transactions on applied superconductivity* (2010). DOI: 10.1109/TASC.2010.2040167.

[11] H. Müller et al. "Status of the Super-FRS magnet devlopment for FAIR." In: *Proc. 6th International Particle Accelerator Conference (IPAC'15)* (2015). DOI: 10.18429/JACoW-IPAC2015-WEPMA019.

[12] G. Golluccio et al. "Instruments and methods for the magnetic measurement of the Super-FRS magnets." In: *7th International Particle Accelerator Conference* (2016). DOI: 10.18429/JACoW-IPAC2016-TUPMB037.

[13] W. Yang et al. "Magnetic Field Measurement for Synchrotron Dipole Magnets of Heavy-Ion Therapy Facility in Lanzhou." In: *IEEE Transactions on Applied Superconductivity* (2014). DOI: 10.1109/TASC.2013.2289953.

[14] B. Auchmann, S. Kurz, and S. Russenschuck. "A note on faraday paradoxes." In: *IEEE Transactions on Magnetics* (2014). DOI: 10.1109/TMAG.2013.2285402.

[15] Stephan Russenschuck. *Personal Communication*. 2019.

[16] *Mercury II® 6000 Series Encoder - Sensor Installation Manual and Reference Guide*. Mercury Encoder 6500. Rev. 181127. Celera Motion. 2018.

[17] P. Arpaia et al. "Performance of a fast digital integrator in on-field magnetic measurements for particle accelerators." In: *Review of Scientific Instruments* (2012). DOI: 10.1063/1.3673000.

[18] Robin Willink. *Measurement Uncertainty and Probability*. Cambridge University Press, 2013. DOI: 10.1017/CBO9781139135085.

[19] E. Schrüfer, L.M. Reindl, and B. Zagar. *Elektrische Messtechnik: Messung elektrischer und nichtelektrischer Größen*. Carl Hanser Verlag GmbH Co. KG, 2014. DOI: 10.3139/9783446433298.

[20] P. Rogacki et al. "Development of a rotating-coil scanner for superconducting accelerator magnets." In: *20. GMA/ITG-Fachtagung Sensoren und Messsysteme 2019*. 2019. DOI: 10.5162/SENSOREN2019/3.4.3.

[21] P. Arpaia et al. "In situ calibration of rotating sensor coils for magnet testing." In: *Review of Scientific Instruments* 83 (2012). DOI: 10.1063/1.3675578.

[22] P. Arpaia et al. “Offset correction in a digital integrator for rotating coil measurements.” In: *IMEKO World Congress Metrology for green growth*. 2012.

[23] P. Arpaia, V. Inglese, and G. Spiezia. “Performance improvement of a DSP-based digital integrator for magnetic measurements at CERN.” In: *IEEE Transactions on Instrumentation and Measurement* (2009). DOI: 10.1109/TIM.2008.2006723.

[24] P. Arpaia et al. “A Fast Digital Integrator for Magnetic Field Measurements at Cern.” In: *IEEE Instrumentation and Measurement Technology Conference Proceedings*. 2006. DOI: 10.1109/IMTC.2006.328175.

[25] M. Liebsch, S. Russenschuck, and S. Kurz. “Boundary-Element Methods for Field Reconstruction in Accelerator Magnets.” In: *IEEE Transactions on Magnetics* (2020). DOI: 10.1109/TMAG.2019.2952092.

[26] Alfred Mertins. *Signaltheorie*. 2010. DOI: 10.1007/978-3-8348-9381-9.

[27] Holger Wendland. *Error, Stability and Conditioning*. Cambridge University Press, 2017. DOI: 10.1017/9781316544938.003.

[28] S. Russenschuck et al. “Challenges in extracting pseudo-multipoles from magnetic measurements.” In: *Proc. 13th International Computational Accelerator Physics Conference*. 2019. DOI: 10.18429/JACoW-ICAP2018-SUPAG03.

[29] B. Erdelyi, M. Lindemann, and M. Berz. “Differential algebra based magnetic field computations and accurate fringe field maps.” In: *APS April Meeting Abstracts*. 2000.

[30] S. Russenschuck. “Rotating- and translating-coil magnetometers for extracting pseudo-multipoles in accelerator magnets.” In: *COMPEL-The international journal for computation and mathematics in electrical and electronic engineering* (2017). DOI: 10.1108/COMPEL-02-2017-0059.

[31] Melvin Liebsch. *Personal Communication*. 2020.